

Ruthenium(II) Polypyridyl Complexes Containing COUBPY Ligands as Potent Photosensitizers for the Efficient Phototherapy of Hypoxic Tumors

Diego Abad-Montero,[◆] Albert Gandioso,[◆] Eduardo Izquierdo-García,[◆] Sergi Chumillas,[◆] Anna Rovira, Manel Bosch, Mireia Jordà-Redondo, Davor Castaño, Joaquín Bonelli, Valentin V. Novikov, Alba Deyà, José Luis Hernández, Jorge Galino, Marta E. Alberto, Antonio Francés-Monerris, Santi Nonell, Gilles Gasser,* and Vicente Marchán*

Cite This: *J. Am. Chem. Soc.* 2025, 147, 7360–7376

Read Online

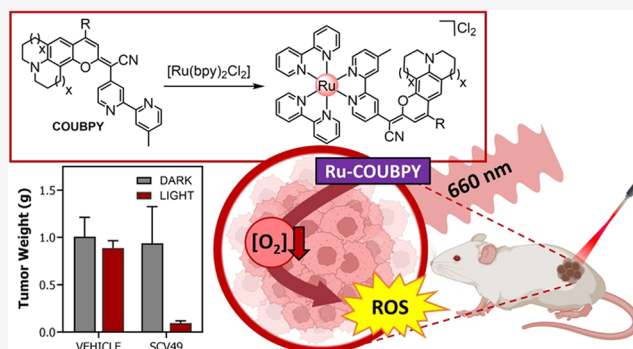
ACCESS |

Metrics & More

Article Recommendations

Supporting Information

ABSTRACT: Hypoxia, a hallmark of many solid tumors, is linked to increased cancer aggressiveness, metastasis, and resistance to conventional therapies, leading to poor patient outcomes. This challenges the efficiency of photodynamic therapy (PDT), which relies on the generation of cytotoxic reactive oxygen species (ROS) through the irradiation of a photosensitizer (PS), a process partially dependent on oxygen levels. In this work, we introduce a novel family of potent PSs based on ruthenium(II) polypyridyl complexes with 2,2'-bipyridyl ligands derived from COUPY coumarins, termed COUBPYs. Ru-COUBPY complexes exhibit outstanding *in vitro* cytotoxicity against CT-26 cancer cells when irradiated with light within the phototherapeutic window, achieving nanomolar potency in both normoxic and hypoxic conditions while remaining nontoxic in the dark, leading to impressive phototoxic indices (>30,000). Their ability to generate both Type I and Type II ROS underpins their exceptional PDT efficiency. The lead compound of this study, SCV49, shows a favorable *in vivo* pharmacokinetic profile, excellent toxicological tolerability, and potent tumor growth inhibition in mice bearing subcutaneous CT-26 tumors at doses as low as 3 mg/kg upon irradiation with deep-red light (660 nm). These results allow us to propose SCV49 as a strong candidate for further preclinical development, particularly for treating large hypoxic solid tumors.



INTRODUCTION

Hypoxia, or low oxygen concentration, is a feature commonly found in aggressive solid tumors, such as glioblastoma, colorectal, pancreatic, and breast cancers.¹ While the oxygen level in normal tissues is typically above 40 mmHg, hypoxic areas within tumors have oxygen levels below 10 mmHg (equivalent to 1–2% O₂ or even below) due to rapid tumor cell proliferation and abnormal blood vessel formation.² This low-oxygen environment promotes tumor angiogenesis, metastasis, and resistance to conventional treatments like chemotherapy, radiotherapy, and immunotherapy, leading to poorer patient outcomes and a higher risk of cancer recurrence.^{3,4}

Photodynamic therapy (PDT) is a clinically approved method for eradicating tumors and/or tumor vasculature that uses light-responsive drugs known as photosensitizers (PSs).^{5–7} This technique involves administering locally or systemically a nontoxic dose of a PS, followed by light activation directly at the tumor site, producing a series of highly cytotoxic reactive oxygen species (ROS) that cause cell damage and ultimately lead to tumor cell death. Besides these

direct effects, PDT-stimulated immune response also induces local acute inflammation, whereas the phototriggered vascular damage can lead to tumor infarction.^{8,9} PDT is also effective at treating other conditions, such as actinic keratosis, age-related macular degeneration, and some fungal and microbial infections. PSs can operate through two main mechanisms: Type I and Type II. On the one hand, the Type II mechanism involves sensitizing singlet oxygen (¹O₂) through an energy-transfer process from the excited triplet state of the PS to molecular oxygen in the ground state. On the other hand, the Type I PDT mechanism is based on electron transfer reactions that generate a variety of ROS, such as superoxide ([•]O₂⁻) and hydroxyl ([•]OH) radicals. While the effectiveness of Type II

Received: October 27, 2024

Revised: January 31, 2025

Accepted: February 3, 2025

Published: February 15, 2025



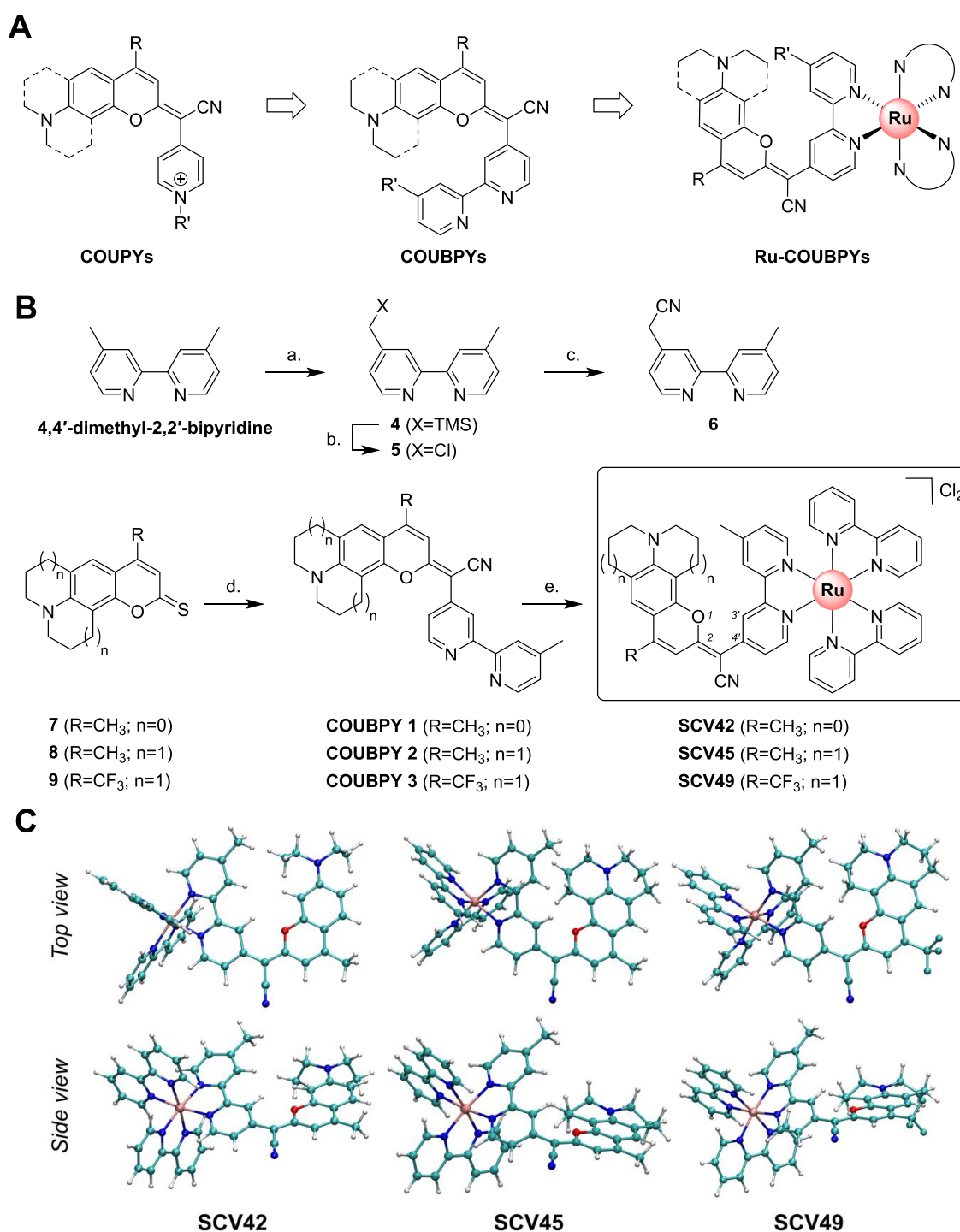


Figure 1. Rational design, synthesis, and characterization of Ru-COUBPY complexes. (A) Design of the COUBPY ligands and of the corresponding Ru(II) polypyridyl complexes. (B) Synthetic route for the preparation of COUBPY ligands 1–3 and Ru-COUBPY complexes **SCV42**, **SCV45**, and **SCV49**. Reagents and conditions: (a) (1) LDA, THF, $-78\text{ }^{\circ}\text{C}$, 1 h, (2) TMSCl, $-78\text{ }^{\circ}\text{C}$, 10 s, (3) EtOH, $-78\text{ }^{\circ}\text{C}$ to rt, 1 h, 76%; (b) $(\text{CCl}_3)_2$, CsF, ACN, $60\text{ }^{\circ}\text{C}$, 3.5 h, 57%; (c) KCN, 18-crown-6, ACN, rt to $50\text{ }^{\circ}\text{C}$, overnight, 64%; (d) (1) NaH, **6**, ACN, rt, 2 h, (2) AgNO_3 , rt, 2 h, 20–75%; (e) $[\text{Ru}(\text{bpy})_2\text{Cl}_2]$, EtOH-H₂O (3:1), $80\text{ }^{\circ}\text{C}$, overnight, 62–93%. (C) Ground-state geometries of Ru-COUBPY complexes in ACN optimized by the PBE0/6-31+G(d,p)/SDD method in ACN.

PDT relies heavily on surrounding oxygen levels, the Type I PDT mechanism can remain effective even in low-oxygen environments, presenting a promising approach for addressing the hypoxia problem in cancer therapy.^{10,11}

Compared to conventional cancer treatments, PDT offers several advantages, such as noninvasiveness and spatial and temporal selectivity, which are associated with much milder

and localized side effects. However, it still faces significant challenges that limit its broad clinical application. To date, most marketed photosensitizers based on the well-known tetrapyrrolic scaffold, including porphyrins, chlorins, and phthalocyanines, share three main limitations: (i) dark toxicity, which causes undesired side effects and limits the dose patients can receive; (ii) reduced effectiveness in hypoxic tumors due to

Table 1. Photophysical Properties and Singlet Oxygen Quantum Yields of Ru-COUBPY Complexes in ACN at Room Temperature^a

	spectroscopic properties				singlet oxygen quantum yield Φ_{Δ}		
	$\lambda_{\text{abs}}/\text{nm}$ ($\epsilon/\text{mM}^{-1} \text{ cm}^{-1} \times 10^3$)	$\lambda_{\text{em}}/\text{nm}$ (460 nm)	$\lambda_{\text{em}}/\text{nm}$ (520 nm)	$\lambda_{\text{em}}/\text{nm}$ (600 nm)	τ air/ns	direct (532 nm)	indirect (505 nm)
SCV42	289 (53), 472 (17), 520 (22), 555 (25)	527, 612	599, 667	-	3.7, 116	0.33	0.48
SCV45	289 (43), 460 (11), 515 (12), 564 (14)	523, 617	616	632	3.8, 126	0.19	0.32
SCV49	289 (55), 461 (16), 571 (20)	519	664	667	5.5, 148	0.12	0.21

^aAbsorption (λ_{abs}) maxima wavelengths, molar absorption coefficients at λ_{abs} (ϵ), emission (λ_{em}) maxima wavelengths at the indicated λ_{exc} , emission lifetimes (τ), and singlet oxygen quantum yield (Φ_{Δ}) by direct and indirect method upon excitation at the indicated wavelengths.

their reliance on the Type II PDT mechanism; and (iii) activation by short-wavelength light, limiting tissue penetration and access to larger tumors. Furthermore, this kind of PSs often suffer from poor water solubility and prolonged skin photosensitivity and requires complex synthetic processes that produce mixtures of compounds. As the incidence of cancer continues to rise worldwide, the global PDT market is rapidly expanding and requires alternative PSs beyond traditional tetrapyrrolic scaffolds. Ideally, these new PSs should be activatable by long-wavelength light (deep-red to near-infrared, NIR) and work through both Type I and Type II mechanisms to effectively treat large hypoxic solid tumors.^{12–20} Additionally, to enhance therapeutic efficacy and minimize toxicity, an ideal PS should preferentially accumulate in key subcellular organelles, such as mitochondria, that are essential for several crucial cellular processes.^{21–23}

Metal-based PSs hold great promise for anticancer PDT due to their unique properties, as illustrated by the entrance of the Ru(II) polypyridyl complex TLD-1433 in clinical trials.²⁴ These transition metal complexes feature multiple electronic excited states that enable efficient ROS-generating photo-reactions, and their modular three-dimensional architecture allows for easy modification of their chemical structures to optimize photophysical, photochemical, and photobiological properties through the careful selection of appropriate ligand–metal combinations.^{25–28} However, despite recent advances, particularly with cyclometalated Ir(III) complexes as well as Ru(II) and Os(II) polypyridyl complexes,^{29–40} most metal-based PSs still share some of the drawbacks of traditional tetrapyrrolic-based PSs, including high dark toxicity, reduced efficacy under hypoxia, and activation with relatively short-wavelength light. Photoactivated chemotherapy (PACT) using Ru(II) complexes also offers great potential for the treatment of hypoxic tumors due to its oxygen-independent mechanism, which is based on the release of a bioactive cargo molecule from a caged compound upon light irradiation.^{41–44} Additionally, several strategies have been developed to enhance PDT efficiency in hypoxic tumors by increasing oxygen availability within the tumor microenvironment.^{45–47}

Organic fluorophores, particularly those operating in the optical window of biological tissues (600–900 nm), are essential tools for bioimaging applications and phototherapies. We recently developed a new family of coumarin-based deep-red/NIR fluorophores, known as COUPYs, based on the incorporation of a cyano(1-alkyl-4-pyridin-1-ium)methylene group at position 2 of the coumarin backbone (Figure 1A).⁴⁸ The photophysical properties of COUPY dyes can be easily tuned with minimal structural modifications,^{49,50} making them suitable for fluorescently labeling biomolecules.^{51,52} Additionally, COUPY fluorophores show significant potential as PDT

agents, whether in their free form,⁵³ nanoencapsulated,⁵⁴ or when conjugated to transition metal complexes.^{55–58}

Building on these precedents, in this work, we describe the first development of a new family of PSs based on Ru(II) polypyridyl complexes incorporating unprecedented 2,2'-bipyridyl ligands derived from COUPY coumarins, termed COUBPYs, in the metal coordination sphere (Figure 1A). These PSs exhibit exceptional *in vitro* cytotoxicity against cancer cells upon irradiation with light within the phototherapeutic window, under both normoxic and hypoxic conditions, while remaining nontoxic in the dark. The strong phototoxic activity of Ru-COUBPY PSs under hypoxia can be attributed to their ability to simultaneously photogenerate Type I and Type II ROS, providing a distinct advantage over current marketed PSs that primarily rely on the latter mechanism. Moreover, the results from the *in vivo* safety and efficacy studies in mice underscore the potential of Ru-COUBPY PSs, particularly the lead compound SCV49 (Figure 1B), as promising candidates for further preclinical development in the PDT treatment of challenging hypoxic tumors.

RESULTS AND DISCUSSION

Design, Synthesis, and Chemical Characterization of Ru-COUBPY PSs. Ru-COUBPY complexes were successfully obtained following the synthetic strategies depicted in Figure 1B. First, the required COUBPY ligands 1–3 incorporating 2,2'-bipyridine (bpy) at position 2 of the coumarin skeleton were synthesized through a condensation reaction between suitable thiocoumarin derivatives and a 2,2'-bipyridyl acetonitrile precursor (6), which was prepared from the commercially available 4,4'-dimethyl-2,2'-bipyridine. Based on previous structure–photophysical property relationships within the COUPY scaffold,^{50,57} the *N,N*-dialkylamino benzene group in COUBPY 1 was replaced with a julolidine moiety (2 and 3) to achieve a redshift in the absorption and emission maxima. Similarly, the incorporation of a strong electron-withdrawing CF₃ group at position 4 of the coumarin backbone in COUBPY 3 was anticipated to cause a further redshift and enhance photostability.^{48,49} Three Ru-COUBPY complexes, SCV42, SCV45 and SCV49, were assembled by reaction between COUBPY ligands 1, 2 and 3, respectively, and a Ru(II) dichlorido complex precursor, [Ru(bpy)₂Cl₂], in a EtOH/H₂O 3:1 (v/v) mixture at 80 °C overnight. The complexes were easily isolated by silica column chromatography with good yields (62–93%) and fully characterized by 1D ¹H and ¹³C NMR, 2D ¹H,¹H NOESY NMR and HRMS. The purity of the products was assessed by reversed-phase HPLC-MS analysis, revealing a single peak in all cases (Figure S1). Interestingly, as previously found in COUPY fluorophores, the ¹H NMR spectra of Ru-COUBPY complexes showed two sets of proton signals, the proportion of which

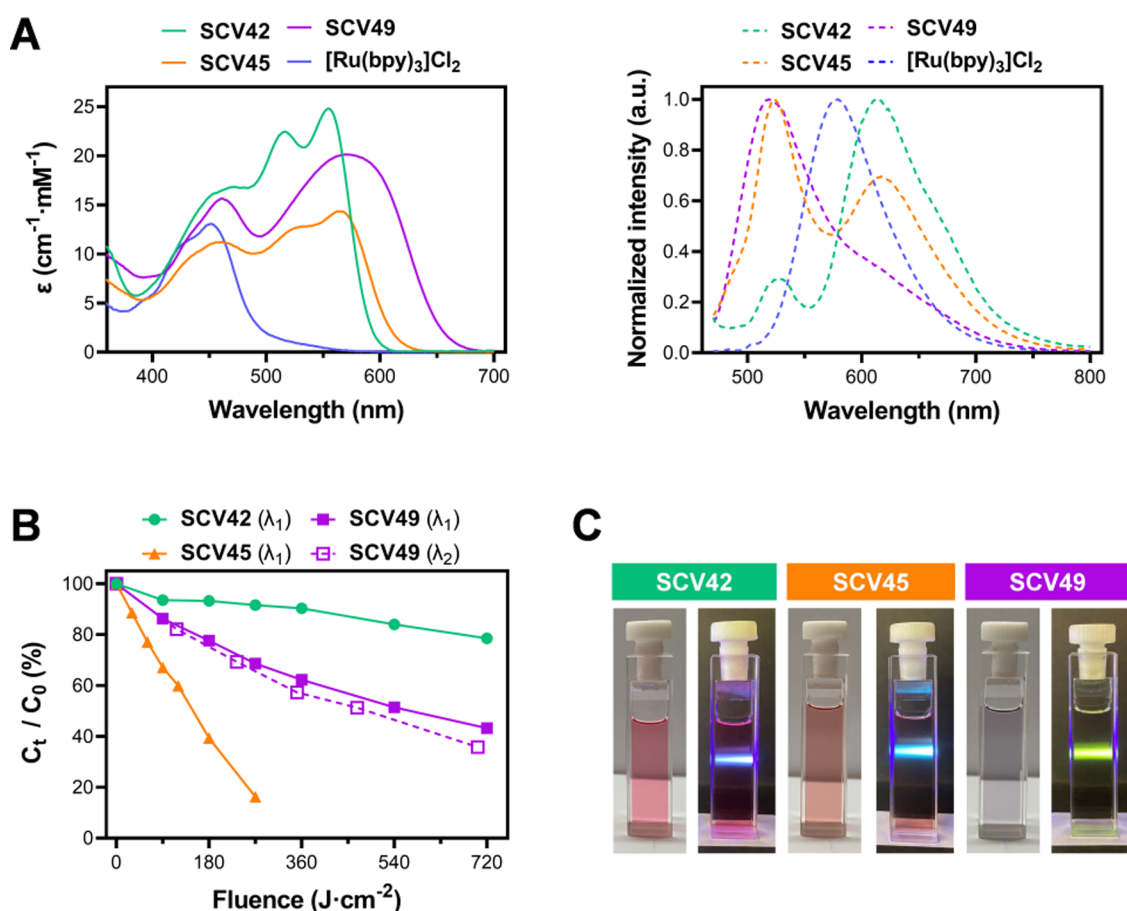


Figure 2. Photophysical characterization of Ru-COUBPY complexes. (A) Absorption (left panel) and emission ($\lambda_{\text{exc}} = 460$ nm) (right panel) spectra of the Ru-COUBPY complexes in ACN. (B) Photostability of the complexes in supplemented cell culture medium at 37 °C after irradiation with green ($\lambda_1 = 505 \pm 35$ nm, 100 mW cm^{-2}) or red ($\lambda_2 = 620 \pm 15$ nm; 130 mW cm^{-2}) light. C_0 and C_t represent the concentration of the compound at the beginning of the experiment ($t = 0$) and at various time points throughout the experiment, respectively. (C) Photographic images of Ru-COUBPY complex solutions (50 μM) in DCM under daylight (left panel) and in the dark (right panel) upon irradiation with a blue laser (405 nm).

remained nearly the same as in the case of the free COUBPY ligand ($\approx 90\text{--}95:10\text{--}5$). The same duplicity was found in the ^{13}C and ^{19}F (only for **3** and **SCV49**) NMR spectra. The presence of exchange cross-peaks in the NOESY spectra (e.g., see Figure S23 for **SCV42**) confirmed the existence of rotamers in solution around the exocyclic double bond connecting the C2 of the coumarin moiety and the C4 of the bipyridine, which accounts for the strong electronic delocalization along the π -system of the COUBPY ligand. In all cases, the presence of characteristic NOE cross-peaks confirmed that the *E* rotamer was the major species in solution (Figures S20–S25). In coherence with this finding, the molecular models of Ru-COUBPY complexes shown in Figure 1C have been built in the predominant *E* disposition.

Photophysical Characterization: Experimental and Computational Studies. The photophysical properties of Ru-COUBPY complexes were experimentally measured in acetonitrile (ACN) at room temperature. As shown in Table 1 and Figure 2A, the absorption spectra of the Ru-COUBPY complexes differ significantly from that of the reference Ru(II) polypyridyl complex $[\text{Ru}(\text{bpy})_3]\text{Cl}_2$, due to the replacement of one bpy ligand with COUBPY ligands. The strong absorption band around 450 nm in $[\text{Ru}(\text{bpy})_3]\text{Cl}_2$, assigned to the metal-to-ligand charge transfer (MLCT) transition, is slightly red-shifted in the Ru-COUBPY complexes. Furthermore, the

spectra of the Ru-COUBPYs exhibit additional bands beyond 500 nm, that are not present in the $[\text{Ru}(\text{bpy})_3]^{2+}$ molecule, and in which computations reveal a contribution from COUBPY ligands (*vide infra*). In the cases of **SCV42** and **SCV45**, two sharp almost fused bands appear in the 500–600 nm region. Remarkably, **SCV49** exhibits a broader band centered at 570 nm with some weak absorption extending beyond 700 nm.

The emission properties of the Ru-COUBPY complexes were investigated by using excitation at three different wavelengths (460, 520, and 600 nm) (Figures 2A and S26). When excited within the COUBPY absorption band ($\lambda_{\text{exc}} = 520$ or 600 nm), all three complexes exhibit emission signals in the far-red to NIR region. As expected, **SCV49** shows a significantly red-shifted emission maximum ($\lambda_{\text{em}} = 667$ nm) upon excitation at 600 nm, compared to **SCV42** and **SCV45**. However, it is worth noting that the spectra of the Ru-COUBPY complexes are not the simple sum of those of $[\text{Ru}(\text{bpy})_3]^{2+}$ and the appended coumarins, indicating some degree of mixing of their excited states. Indeed, the wavelength dependence of the emission spectra reflects different deactivation pathways depending on the nature of the originally excited chromophore. Time and spectrally resolved luminescence spectroscopy nevertheless confirmed the presence of coumarin and $[\text{Ru}(\text{bpy})_3]^{2+}$ features. Specifically, two

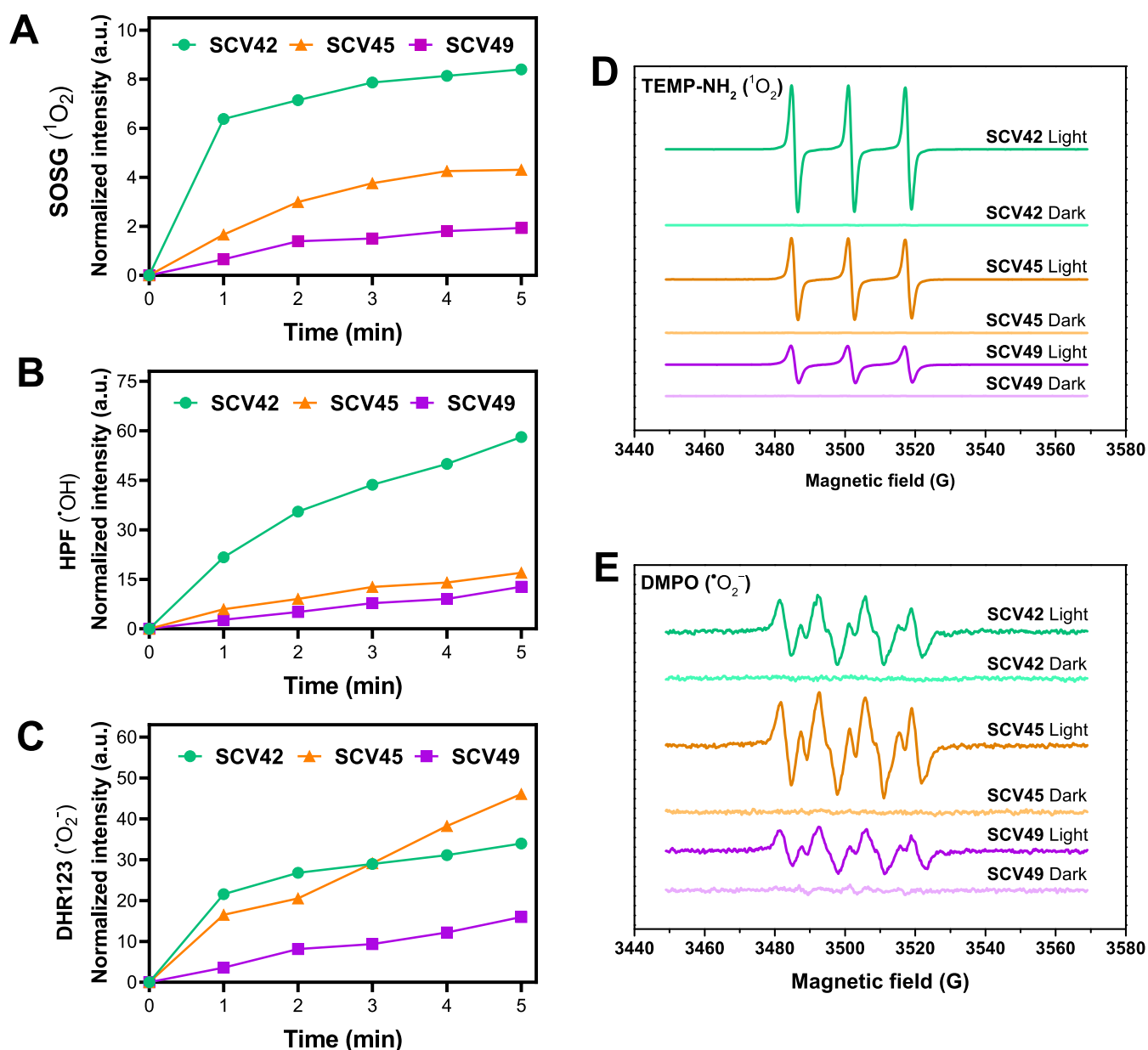


Figure 3. Photogeneration of ROS by Ru-COUBPY complexes studied using specific fluorogenic probes (A–C) and EPR spectroscopy (D–E). Left panels: Increase in fluorescence emission of probes SOSG (5 μM) (A), HPF (5 μM) (B), and DHR123 (10 μM) (C) occurred upon irradiation of Ru-COUBPY complexes (10 μM) in PBS (2% DMSO). Right panels: EPR spectra of Ru-COUBPY complexes trapped by 4-amino-TEMP (D) or DMPO (E) in MeOH, measured in the dark and after green light irradiation.

luminescence decays could be observed for the three Ru-COUBPY complexes with short (3.7–5.5 ns) and long (116–148 ns) components upon excitation at 405 nm in air-saturated acetonitrile solutions (Figure S27), which can be loosely assigned to the fluorescence of the appended coumarin moiety and the phosphorescence of the ruthenium complex core, respectively.

To gain more insight into the spectroscopic properties of Ru-COUBPY complexes, their ground-state and excited singlet and triplet state properties in ACN were studied using density functional theory (DFT) and time-dependent (TD)-DFT calculations. As shown in Figure 1C, the Ru metal center adopts an octahedral disposition, whereas the coumarin fragment is quasi coplanar to the bpy ligand to which it is attached to a different extent depending on the complex. The values of the O1–C2–C4'–C3' dihedral angle (see atom

numbering in *italics* in Figure 1B) are 13.8, 30.8, and 31.2° for SCV42, SCV45, and SCV49, respectively, and quantify the relative torsion between the bpy and the coumarin moiety. The higher values for SCV45 and SCV49 are coherent with the larger steric hindrance induced by the julolidine ring in the latter two compounds.

The absorption properties in the visible range are rationalized in Tables S1–S3 and Figures S28–S31. The lowest energy bands experimentally centered at 555, 564, and 571 nm for SCV42, SCV45, and SCV49, respectively (Table 1), have been computed at slightly shorter wavelengths (Tables S1–S3) and have been fully characterized as MLCT bands in the first two cases and with a mixed MLCT/ IL_{cou} character for SCV49 as a result of the impact of the CF_3 substituent in the $\pi \rightarrow \pi^*$ absorption in the COUBPY moiety. This is clearly revealed by the natural transition orbitals

Table 2. Thermodynamics [$\Delta E = E(\text{products}) - E(\text{reactants})$] of the Type I PDT Reactions Computed with the Vertical Electron Affinities (VEAs) and Vertical Ionization Potential (VIP) Values Shown in Tables S5–S7^a

reaction	system		
	42	45	49
${}^1\text{SCV}^{2+} + {}^3\text{O}_2 \rightarrow {}^2\text{SCV}^{3+} + {}^2(\bullet\text{O}_2^-)$ (1)	2.00	1.83	1.97
${}^3\text{SCV}^{2+} + {}^3\text{O}_2 \rightarrow {}^2\text{SCV}^{3+} + {}^2(\bullet\text{O}_2^-)$ (2)	-0.03	-0.17	0.24
${}^1\text{SCV}^{2+} + {}^1\text{SCV}^{2+} \rightarrow {}^2\text{SCV}^{3+} + {}^2\text{SCV}^+$ (3)	0.50	0.42	0.55
${}^3\text{SCV}^{2+} + {}^3\text{SCV}^{2+} \rightarrow {}^2\text{SCV}^{3+} + {}^2\text{SCV}^+$ (4)	-1.54	-1.58	-1.18
${}^2\text{SCV}^+ + {}^3\text{O}_2 \rightarrow {}^1\text{SCV}^{2+} + {}^2(\bullet\text{O}_2^-)$ (5)	-0.53	-0.59	-0.31
${}^3\text{COU} + {}^1[\text{Ru}(\text{bpy})_2(\text{dmbpy})]^{2+} \rightarrow {}^2\text{COU}^+ + {}^2[\text{Ru}(\text{bpy})_2(\text{dmbpy})]^{2+}$ (6)	0.06	-0.04	0.44
${}^2[\text{Ru}(\text{bpy})_2(\text{dmbpy})]^{2+} + {}^3\text{O}_2 \rightarrow {}^1[\text{Ru}(\text{bpy})_2(\text{dmbpy})]^{2+} + {}^2(\bullet\text{O}_2^-)$ (7)	-0.27 ^b		
${}^2[\text{Ru}(\text{bpy})_2(\text{dmbpy})]^{2+} + {}^2\text{COU}^+ \rightarrow {}^1[\text{Ru}(\text{bpy})_2(\text{dmbpy})]^{2+} + {}^1\text{COU}$ (8)	-1.81	-1.64	-1.85
${}^3\text{SCV}^{2+} + {}^2(\bullet\text{O}_2^-) \rightarrow {}^2\text{SCV}^+ + {}^3\text{O}_2$ (9)	-1.50	-1.41	-1.42

^aMolecular models of ${}^2[\text{Ru}(\text{bpy})_2(\text{dmbpy})]^{2+}$ and coumarin fragments COU42^+ , COU45^+ , and COU49^+ are shown in Figure S50. Values in eV. The number in the superscript at the left indicates spin, while the superscript at the right indicates the molecular charge. Thus, ${}^1\text{SCV}^{2+}$ stands for the Ru-COUBPY complex in the singlet ground state (S_0) with a total charge of +2, ${}^2\text{SCV}^{3+}$ refers to the first doublet state (D_1) of the oxidized complex with a total charge of +3, and so on. ^bThis reaction is not specific to any COU structure since only the Ru center, the (bpy)₂ and dmbpy ligands, and molecular oxygen are involved.

(NTOs)^{59,60} and from inspection of the quantitative wave function analysis⁶¹ displayed in Figures S28–S31. Indeed, Figure S29 corroborates that the Ru(II)-coordinated ligands local components (blue color) dominate the lowest-energy S_1 states in all cases except SCV49, in which the increasing contribution of the COUBPY intraligand (IL) charge transfer component (red color) is connected with the red-shift of the absorption band observed going from SCV42 to SCV49. The bands experimentally found at 520 and 515 nm for SCV42 and SCV45, missing in SCV49, are well reproduced by the singlet–singlet transition to S_3 computed at 507 and 513 nm, which mixes MLCT and IL_{cou} character. A non-negligible COUBPY → Ru(II) complex charge transfer component is also detected in both transitions, although it is larger for SCV45 with respect to SCV42 (Figure S29). Several transitions around the most intense one computed at 469 nm (S_6) contribute to the broad shoulder experimentally recorded at ~459 nm for SCV42 and, analogously, the same band at 460 nm for SCV45 can be attributed to the S_6 state computed at 479 nm. A similar absorption feature in this region characterizes the spectrum of SCV49 in which two transitions of almost equal intensities, computed at 441 and 448 nm, are responsible for the band registered experimentally at 461 nm. In all cases, quantitative wave function analysis and inspection of the NTOs (Figures S28–S31) reveal a dominant MLCT/IL_{cou} nature for the band in this region.

Dark and Light Stability of Ru-COUBPY Complexes in Biological Media. The stability of the Ru-COUBPY complexes was investigated in a complete cell culture medium (DMEM supplemented with 10% FBS), both in the dark and under visible light irradiation. According to HPLC-MS analysis, all compounds remained completely stable after 24 h of incubation in the dark at 37 °C (Figures S32–S35). Furthermore, both SCV42 and SCV49 exhibited remarkable photostability after 1 h of irradiation with green light (505 ± 35 nm, $100 \text{ mW}\cdot\text{cm}^{-2}$, 360 J cm^{-2}), with SCV42 showing greater resistance to photodegradation than SCV49 (Figures 2B and S36–S39). Surprisingly, SCV45 was fully photobleached after the same irradiation time. This suggests that the

incorporation of the CF₃ group at position 4 of the coumarin backbone in SCV49 enhances the photostability, whereas the substitution of the 7-dialkylamino group with a julolidine moiety has a detrimental effect. Furthermore, SCV49 experienced less than 35% photobleaching after 1 h of irradiation with red light (620 ± 15 nm; 130 mW cm^{-2} , 468 J cm^{-2}). Noteworthy, all three Ru-COUBPY complexes were found completely photostable (<3% photodegradation by HPLC-MS analysis) under the typical fluences used in *in vitro* photocytotoxicity experiments (e.g., 9 J cm^{-2} with 540 and 645 nm light; *vide infra*).

Photochemical Characterization: Experimental and Computational Studies. The ability of Ru-COUBPY complexes to photogenerate various types of ROS was evaluated by using a combination of spectroscopic methods. First, singlet oxygen sensor green (SOSG) was used to confirm that the complexes can sensitize singlet oxygen (${}^1\text{O}_2$) upon visible light irradiation (Figure 3A). As expected, the increase in the SOSG fluorescence signal observed during light irradiation of the Ru-COUBPY complexes was suppressed in the presence of the selective scavenger sodium azide (Figure S41). Then, singlet oxygen quantum yields (Φ_Δ) were determined either by direct observation of the ${}^1\text{O}_2$ phosphorescence ($\lambda_{\text{exc}} = 355$ or 532 nm) (Figure S42), or by using an indirect method with 1,3-diphenylisobenzofuran (DPBF) as a ${}^1\text{O}_2$ scavenger, and $[\text{Ru}(\text{bpy})_3]\text{Cl}_2$ or methylene blue (MB) as standards (Figures S43–S44). As shown in Tables 1 and S4, both methods confirmed that SCV42 is more efficient at sensitizing ${}^1\text{O}_2$ than SCV45 or SCV49, which reproduced the results with SOSG. The fact that the singlet oxygen quantum yields determined by the indirect method using DPBF are slightly higher than those determined by measuring ${}^1\text{O}_2$ phosphorescence can be attributed to its ability to react with ROS other than ${}^1\text{O}_2$ such as superoxide.⁶² The use of two fluorogenic probes, dihydrorhodamine 123 (DHR123) and hydroxyphenyl fluorescein (HPF), confirmed that Ru-COUBPY complexes can also generate superoxide anion radicals ($\bullet\text{O}_2^-$) and hydroxyl radicals ($\bullet\text{OH}$), respectively, upon green light irradiation. This was further

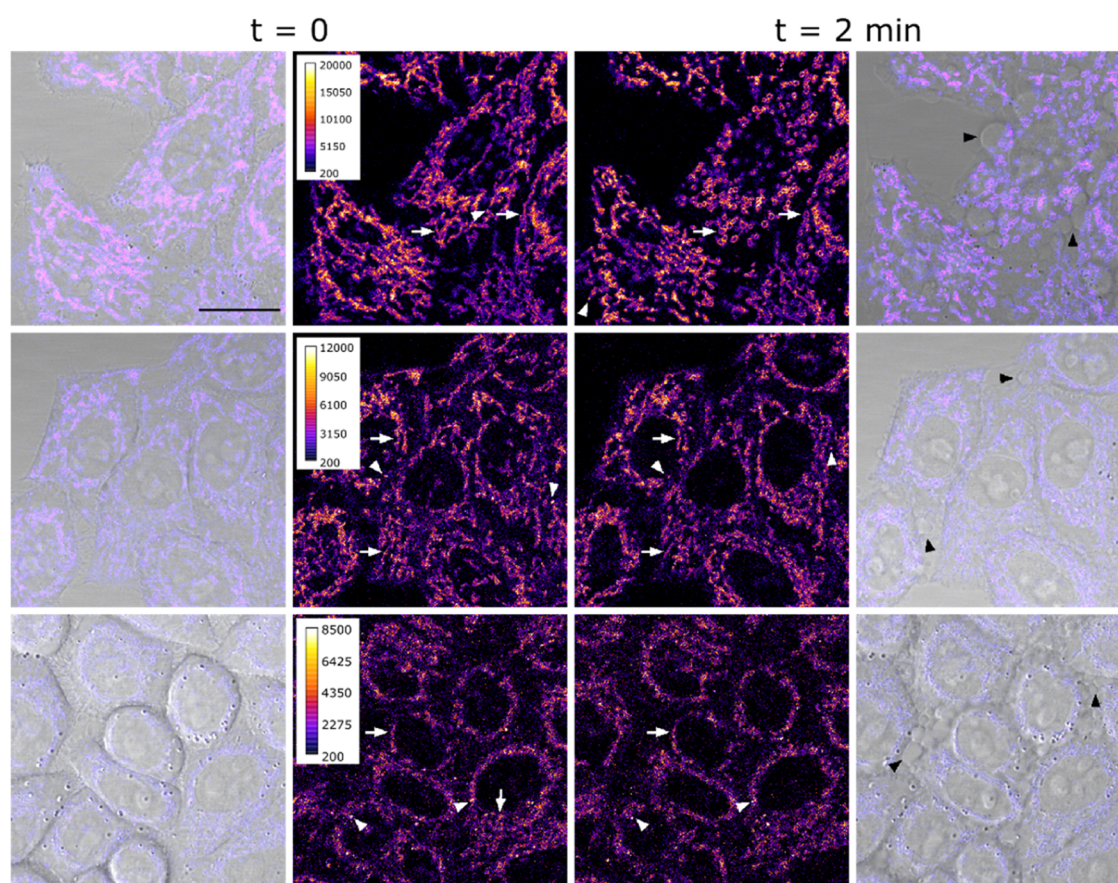


Figure 4. Cellular uptake studies of Ru-COUBPY complexes in living HeLa cells by confocal microscopy. Single confocal planes of HeLa cells incubated with the compounds SCV42 (top panel), SCV45 (center panel), and SCV49 (bottom panel) for 30 min ($10\ \mu\text{M}$) at $37\ ^\circ\text{C}$, imaged at $t = 0$ and after 2 min of first observation. Excitation was performed with a 514 nm laser line. White arrows point out mitochondria and white arrowheads point out vesicle staining. Black arrowheads on the right column indicate cell blebbings. Scale bar: $20\ \mu\text{m}$. LUT for fluorescence images: Fire. Intensity calibration bars are shown in the left central column. Left and right columns: merge of compound and brightfield images.

validated by the suppression of the probe fluorescence signal in the presence of specific scavengers (i.e., tiron for $\bullet\text{O}_2^-$ and terephthalic acid for $\bullet\text{OH}$) (Figures 3B,C and S45–S48). Once again, SCV42 demonstrated greater efficiency in generating both $\bullet\text{O}_2^-$ and $\bullet\text{OH}$ radicals compared to those of its julolidine-containing counterparts. To our delight, SCV49 photogenerates $^1\text{O}_2$, $\bullet\text{O}_2^-$ and $\bullet\text{OH}$ radicals even under red light irradiation (Figures S41, S46, and S48).

Further evidence for the light-induced generation of ROS by Ru-COUBPY complexes was provided by electron paramagnetic resonance (EPR). In these experiments, 4-amino-2,2,6,6-tetramethylpiperidine (4-amino-TEMP) and 5,5-dimethyl-1-pyrroline-*N*-oxide (DMPO) were used as spin traps to detect the production of $^1\text{O}_2$ and $\bullet\text{O}_2^-$, respectively, upon green light irradiation. The ability of Ru-COUBPYs to photogenerate $^1\text{O}_2$ was confirmed by the observation of the characteristic EPR triplet signal (peak integral ratio 1:1:1, Figure 3D), corresponding to the TEMPO spin adduct. Similarly, the appearance of the diagnostic signal for the DMPO- $\bullet\text{O}_2^-$ (peak integral ratio 1:1:1:1) adduct confirmed the photogeneration of $\bullet\text{O}_2^-$ (Figure 3E). No paramagnetic signal was detected in the dark, demonstrating that the production of ROS is a strictly light-induced process. As shown in Figure 3, there is a good correlation between the intensity of the EPR signals and the relative ability of Ru-COUBPY complexes to photogenerate $^1\text{O}_2$ and $\bullet\text{O}_2^-$. Again, the

photogeneration of $^1\text{O}_2$ and $\bullet\text{O}_2^-$ by SCV49 upon red light irradiation was also confirmed by EPR (Figure S49).

In order to gain more insight into the ability of Ru-COUBPY complexes to photogenerate Type I ROS, theoretical methods were used to study PDT electron transfer mechanisms. Thermodynamics of the characteristic electron transfer reactions of Type I PDT are compiled in Table 2. Electron transfer in the dark (1) is highly endothermic, in agreement with the absence of ROS formation in the dark (Figures 3E and S49). Direct electron transfer to O_2 (2) in the triplet state is however favorable for SCV45 ($\Delta E = -0.17\ \text{eV}$) and SCV42 ($\Delta E = -0.03\ \text{eV}$). In striking contrast, reaction 2 is significantly endothermic for SCV49 by $\Delta E = 0.24\ \text{eV}$, due to the weaker electron donor capacities of SCV49. Thus, it is reasonable to conclude that SCV49 is the least efficient system in $\bullet\text{O}_2^-$ photoproduction through reaction 2.

The autoionization in reaction 3, in which one PS molecule is in its excited state and the other one is in the ground state, is not thermodynamically favored for any Ru-COUBPY complex (Table 2). Nevertheless, for the autoionization reaction 4, in which the two PS molecules are in the triplet excited state, the net electron transfer is largely exothermic by $\Delta E < -1\ \text{eV}$ for the three systems (Table 2). Considering that the electron transfer from the reduced PS to the polarized O_2 (5) is clearly favorable for all species, reactions 4 and 5 operate in the three compounds and therefore explain the observed Type I PDT photoreactions throughout the series. Nonetheless, SCV42 and

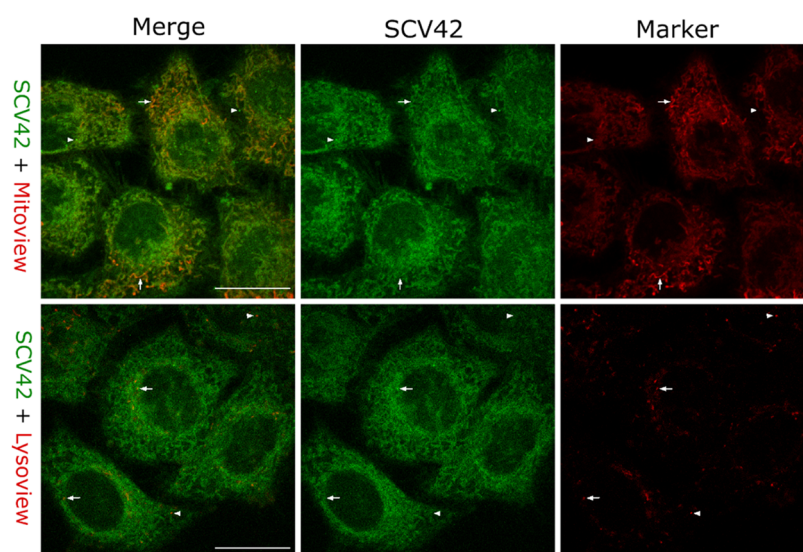


Figure 5. Colocalization studies of SCV42 in living HeLa cells by confocal microscopy. Single confocal planes of HeLa cells incubated with the SCV42 compound (10 μM , green) and Mitoview 650 (0.1 μM , red), or Lysoview 633 (1X, red). Left panel: Merge of the two staining. Center panel: SCV42 signal. Right panel: Mitoview (top) or Lysoview (bottom) signal. White arrows and arrowheads indicate positive and negative colocalization, respectively. Scale bar: 20 μm .

SCV45 have the extra channel (2), which could account for the larger $\cdot\text{O}_2^-$ production observed for these two species with respect to SCV49 (Figure 3B).

The possibility of intramolecular charge transfer from the COUBPY moiety to the Ru^{2+} center complex to generate COUBPY $^+$ and Ru^+ is studied in the triplet state, which dominates slow excited-state processes.⁶³ Figure S51 reveals that the first triplet state (T_1) of SCV42 and SCV45 is a mixture mostly of a local COUBPY excitation (~ 0.4 , red box) and a COUBPY \rightarrow Ru(II) complex component (>0.2 , orange box), whereas for SCV49 the COUBPY local excitation is significantly larger (>0.6) and the charge transfer weight is clearly smaller (<0.2). The NTOs for the T_1 state shown in Figure S52 also confirm this partial COUBPY \rightarrow Ru(II) complex nature, while the energy differences summarized in Table 2 for process (6), which represents the mentioned electron transfers, are close to zero for SCV42 and SCV45, whereas the formation of a Ru(I) center is clearly unfavorable for SCV49. The thermodynamic analysis thus reveals that this superoxide photoproduction mechanism could be operative for SCV42 and SCV45, even more considering that the electron transfer from the reduced $^2[\text{Ru}(\text{bpy})_2(\text{dmbpy})]^+$ fragment to $^3\text{O}_2$ is thermodynamically favorable by $\Delta E = -0.27$ eV [process (7), see Table 2]. Nevertheless, this reaction competes with recombination (8), highly favored thermodynamically. SCV49 is clearly not capable of undergoing intramolecular electron transfer (6), supporting the smaller $\cdot\text{O}_2^-$ production observed for this system (Figure 3B). All in all, although possible, the production of superoxide via Ru(I) through processes (6) and (7) should be considered as a secondary pathway for SCV42 and SCV45 and irrelevant for SCV49.

Table 2 also shows that $\cdot\text{O}_2^-$ can act itself as a reducing agent reacting with the three Ru-COUBPY complexes in the triplet excited states, as illustrated by photoreaction (9). This O_2 “partial recycling”^{64,65} may be one rationale for the high phototoxicity induced by these compounds at low oxygen concentrations.

Cellular Uptake and Subcellular Localization. The cellular uptake of Ru-COUBPY complexes was initially investigated by confocal microscopy in living HeLa cells, taking advantage of the luminescence of the metal complexes for visualization. In all cases, a clear fluorescence signal was detected inside the cells after only 30 min of incubation at a concentration of 10 μM (Figures 4 and S53–S55). While SCV42 and SCV45 displayed a distinctive filamentous staining pattern, suggesting preferential accumulation in the mitochondria, SCV49 exhibited a more diffuse staining pattern with additional localization in intracellular vesicles. A clear indication of the high phototoxicity of Ru-COUBPY complexes was the rapid appearance of membrane blebbing and mitochondrial disintegration, observed after less than 2 min of exposure to the laser light of the confocal microscope.

In order to confirm the subcellular localization of the compounds, a series of colocalization experiments were conducted using the mitochondria, lysosomes, and lipid droplet-specific fluorescent markers Mitoview 650, Lysoview 633, and Lipidspot 610, respectively. As shown in Figure 5, the fluorescence signals of SCV42 and Mitoview 650 showed a strong overlap, supported by high values in Pearson’s correlation coefficient (PCC = 0.80) and Manders’ colocalization coefficients (M1 = 0.59 corresponding to the colocalization of the compound over the Mitoview 650 channel; M2 = 0.78 corresponding to the colocalization of the Mitoview 650 over the compound channel), indicating predominant accumulation in the mitochondria. A similar behavior was observed for the julolidine-containing Ru-COUBPY complex SCV45 (Figure S56). In contrast, the correlation between the signals of Mitoview 650 and SCV49 was weaker, indicating that this Ru-COUBPY complex exhibits slightly reduced specificity for mitochondria (Table S8). This reduced specificity was particularly evident under 405 nm excitation, where SCV49 displayed a more prominent vesicular distribution pattern. Colocalization studies with Lysoview 633 and LipidSpot 610 (Table S8 and Figure S57) confirmed that this vesicular distribution was predominantly associated with lipid droplets.

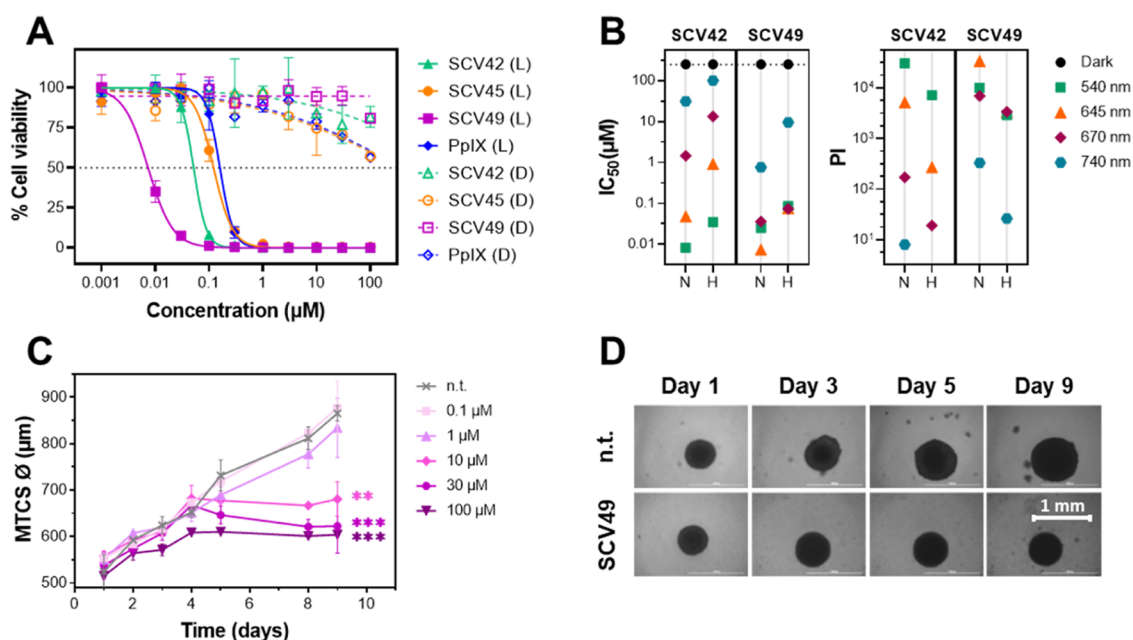


Figure 6. *In vitro* photobiological characterization of Ru-COUBPY complexes in CT-26 2D monolayer cell cultures and 3D multicellular tumor spheroid (MCTS) models. (A) Dose–response curves for SCV42 (green), SCV45 (orange), SCV49 (purple), and PpIX (blue) in CT-26 cells, after 4 h of incubation, upon deep-red light (645 nm, 9.0 J cm⁻²) irradiation (filled symbols) or in the dark (unfilled symbols) under normoxic conditions. (B) Activity plots illustrating the chromatic (photo)cytotoxicity screening of compounds SCV42 and SCV49 in CT-26 cells under green (540 nm, 9.0 J cm⁻²), deep-red (645 nm, 9.0 J cm⁻²), far-red (670 nm, 13.5 J cm⁻²), and NIR (740 nm, 12.6 J cm⁻²) light irradiation, as well as in the dark, under normoxic (21% O₂) and hypoxic (2% O₂) conditions. The plots highlight IC₅₀ values (left panel) and phototherapeutic indexes (PIs) (right panel). Detailed IC₅₀ values with standard deviations and corresponding PI values are provided in Table 4. (C) Evolution of the CT-26 MCTS diameter over a 9-day period. On day 3, MCTSs were treated with varying concentrations of SCV49 (0.1 to 100 μM) or drug-free cell culture medium (n.t.) for 36 h in the dark, followed by 1 h of deep-red light (645 nm, 9.0 J cm⁻²) irradiation. Data are presented as mean ± SD from three replicates. Statistical significance on day 9 was determined using one-way ANOVA followed by Bonferroni's multiple comparison test (Asterisks: ***p* < 0.02, ****p* < 0.002). (D) Brightfield micrographs of CT-26 MCTS treated with SCV49 (100 μM) or drug-free cell culture medium (nt) for 36 h, followed by 1 h of deep-red light (645 nm, 9.0 J cm⁻²) irradiation. Scale bar: 1 mm.

Table 3. (Photo)cytotoxicity of Ru-COUBPY Complexes and of PpIX towards CT-26 Cancer Cells Expressed as IC₅₀ Values (μM) under Normoxia (21% O₂)^a

	PpIX		SCV42		SCV45		SCV49	
	IC ₅₀ (μM)	PI ^b						
dark	>100	-	>250	-	>250	-	>250	-
540 nm	0.320 ± 0.09	>312	0.0082 ± 0.0006	>30,487	0.033 ± 0.004	>7575	0.025 ± 0.002	>10,000
595 nm	0.400 ± 0.01	>250	0.013 ± 0.003	>19,230	0.076 ± 0.007	>3289	0.025 ± 0.004	>10,000
620 nm	0.660 ± 0.210	>151	0.042 ± 0.006	>5952	0.118 ± 0.027	>2118	0.017 ± 0.003	>14,705
645 nm	0.170 ± 0.210	>588	0.048 ± 0.003	>5208	0.117 ± 0.002	>2136	0.0074 ± 0.0006	>33,783
670 nm	0.770 ± 0.200	>129	1.460 ± 0.450	>171	1.11 ± 0.32	>225	0.036 ± 0.003	>6944
740 nm	2.100 ± 0.200	>50	31.3 ± 6.1	>8	32.8 ± 4.6	>7.6	0.76 ± 0.06	>329

^aExperimental conditions: Cells were incubated for 4 h at 37 °C, followed by either 1 h in the dark or irradiation under the specified light conditions. Cell viability was determined after 44 h using the resazurin assay. Irradiation parameters: 540 nm (3.75 mW cm⁻², 9.0 J cm⁻²), 595 nm (0.94 mW cm⁻², 3.4 J cm⁻²), 620 nm (1.88 mW cm⁻², 6.7 J cm⁻²), 645 nm (2.50 mW cm⁻², 9.0 J cm⁻²), 670 nm (3.75 mW cm⁻², 13.5 J cm⁻²), and 740 nm (3.50 mW cm⁻², 12.6 J cm⁻²). ^bPhototherapeutic index (PI) = IC₅₀(dark)/IC₅₀(light).

To evaluate the internalization of Ru-COUBPY complexes in the cellular model intended for upcoming *in vitro* photobiological studies, intracellular ruthenium levels were measured by inductively coupled plasma mass spectrometry (ICP-MS) following the incubation of murine colon cancer cells (CT-26) with SCV42 and SCV49 (4 h, 5 μM). As shown in Figure S58, the intracellular Ru content for SCV42 was slightly higher than that of SCV49, likely due to subtle differences in lipophilicity between the two compounds, as reflected by the experimental octanol–water distribution coefficients. Indeed, according to the logP_{O/W} values (Table S9 and Figure S59), all Ru-COUBPY complexes were

predominantly found in the aqueous phase, with SCV45 and SCV49 being less lipophilic than SCV42, despite the presence of the julolidine moiety. However, all three Ru-COUBPY complexes were more lipophilic than the reference compound [Ru(bpy)₃]Cl₂, lacking the coumarin moiety, which indicates that the incorporation of the COUBPY ligand results in an increase of lipophilicity.

Evaluation of (Photo)cytotoxicity in 2D Monolayer Cancer Cells. After confirming that Ru-COUBPY complexes can photogenerate both Type I and Type II ROS and readily internalize in living cells, preferentially accumulating in the mitochondria, we next evaluated their cytotoxicity against CT-

Table 4. Comparison of the (Photo)cytotoxicity of SCV42 and SCV49 towards CT-26 Cancer Cells under Normoxia (21% O₂) and Hypoxia (2% O₂) Expressed as IC₅₀ Values (μM)^a

	SCV42				SCV49			
	normoxia (21% O ₂)		hypoxia (2% O ₂)		normoxia (21% O ₂)		hypoxia (2% O ₂)	
	IC ₅₀ (μM)	PI ^b	IC ₅₀ (μM)	PI ^b	IC ₅₀ (μM)	PI ^b	IC ₅₀ (μM)	PI ^b
dark	>250	-	>250	-	>250	-	>250	-
540 nm	0.0082 ± 0.0006	>30,487	0.035 ± 0.005	>7143	0.025 ± 0.002	>10,000	0.086 ± 0.011	>2907
645 nm	0.048 ± 0.003	>5208	0.920 ± 0.09	>272	0.0074 ± 0.0006	>33,783	0.076 ± 0.008	>3290
670 nm	1.460 ± 0.450	>171	13.24 ± 3.64	>19	0.036 ± 0.003	>6944	0.074 ± 0.005	>3378
740 nm	31.3 ± 6.1	>8	>100	-	0.76 ± 0.06	>329	9.56 ± 2.15	>26

^aExperimental conditions and irradiation parameters: see legend to Table 3 and SI. ^bPhototherapeutic index (PI) = IC₅₀(dark)/IC₅₀(light).

26 cells under both dark and light conditions. To that end, cells were incubated for 4 h with increasing concentrations of the compounds, and after refreshing the medium, they were either illuminated or kept in the dark. Following a 48-h period after treatment, cell viability was assessed using the resazurin assay, and IC₅₀ values were determined from the dose–response curves (Figures 6A and S60). In all experiments, Protoporphyrin IX (PpIX), the active metabolite of clinically used PS 5-ALA, was used as a reference. The phototoxic index (PI), defined as the ratio of dark to light IC₅₀ values, was used to quantify the phototherapeutic efficiency of the tested compounds. Given the broad absorption band of Ru-COUBPY complexes in the visible spectrum (Figure 2A), a chromatic screening was conducted to evaluate their phototoxicity across seven wavelengths. Using a well-by-well monochromatic LED device, cells were irradiated with green (540 nm, 40 min), yellow (595 nm, 1 h), red (620 nm, 1 h), deep-red (645 nm, 1 h), far-red (670 nm, 1 h), or NIR (740 nm, 1 h) light, with fluences ranging from 3.4 J/cm² (595 nm) to 13.5 J/cm² (670 nm).

As shown in Table 3, Ru-COUBPY complexes displayed no toxicity against CT-26 cells in the dark (IC₅₀ > 250 μM), a key feature for an ideal PDT agent, but became highly toxic after irradiation with visible light. SCV42 exhibited potent nanomolar activity across wavelengths from 540 to 645 nm, with the highest toxicity observed under green light (IC₅₀[540 nm] = 8.2 nM), and slightly lower but still excellent results under red and deep-red light (IC₅₀[620 nm] = 42 nM; IC₅₀[645 nm] = 48 nM). Strikingly, the julolidine-containing complex SCV45 showed significantly reduced phototoxicity compared to its 7-dialkylamino counterpart SCV42, even at wavelengths with higher molar absorptivity (e.g., SCV45: IC₅₀[595 nm] = 76 nM; SCV42: IC₅₀[595 nm] = 13 nM), likely due to lower photostability and reduced efficiency in ROS photogeneration. To our delight, complex SCV49 demonstrated exceptional toxicity under deep-red and far-red light, with IC₅₀ values in the very low nanomolar range (e.g., IC₅₀[645 nm] = 7.4 nM; IC₅₀[670 nm] = 36 nM). Furthermore, SCV49 retained considerable phototoxic activity even under highly penetrating NIR light (IC₅₀[740 nm] = 0.76 μM). This highlights that the bathochromic shift and enhanced photostability resulting from the incorporation of the CF₃ group at position 4 of the coumarin backbone played a crucial role in boosting the overall PDT activity of SCV49. Impressively, all the Ru-COUBPY complexes outperformed the reference PS PpIX at wavelengths below 645 nm, and SCV49 surpassed PpIX even under far-red and NIR irradiation (e.g., PpIX: IC₅₀[670 nm] = 770 nM; SCV49: IC₅₀[670 nm] = 36 nM). The absence of dark toxicity in these PSs, combined with their exceptional toxicity under

light irradiation, resulted in remarkable PI values across the entire visible spectrum. At peak performance, both SCV42 and SCV49 exhibited PI values exceeding 30,000 (e.g., SCV42: PI[540 nm] > 30,487; SCV49: PI[645 nm] > 33,783), positioning Ru-COUBPYs among the most phototherapeutically efficient Ru(II) polypyridyl PSs reported to date.

As discussed earlier, hypoxia is a major factor contributing to the failure of most conventional anticancer therapies. Given the exceptional phototherapeutic profiles of SCV42 and SCV49 under visible light irradiation in normoxic conditions (21% O₂), we next investigated the cytotoxicity of these compounds against CT-26 cells under challenging hypoxic conditions (2% O₂), both in the dark and upon irradiation at four representative wavelengths (540, 645, 670, and 740 nm). The impact of oxygen concentration on phototherapeutic efficiency was measured by using the hypoxia index (HI), defined as the ratio of IC₅₀ values obtained under hypoxic (2% O₂) and normoxic (21% O₂) conditions after light irradiation. Under hypoxia, Ru-COUBPY complexes SCV42 and SCV49 remained nontoxic in the dark (IC₅₀ > 250 μM) while retaining nanomolar cytotoxicity under visible light irradiation (Table 4 and Figures 6B, S61–S62), although their phototoxic activity was slightly diminished compared to normoxic conditions. Once more, SCV42 performed best under green light (IC₅₀[540 nm] = 35 nM, PI > 7143, HI = 4), while SCV49 exhibited excellent phototoxicity under green, deep-red and far-red light (e.g., IC₅₀[670 nm] = 74 nM, PI > 3378, HI = 2), and maintained micromolar activity under NIR light (IC₅₀[740 nm] = 9.56 μM, PI > 26, HI = 12). The exceptional phototoxicity of SCV42 and SCV49, even under hypoxic conditions, likely stems from their ability to simultaneously generate Type I and II ROS in sensitive subcellular structures like mitochondria. These findings further highlight the potential of Ru-COUBPY PSs for treating hypoxic tumors.

Evaluation of (Photo)cytotoxicity in 3D Multicellular Tumor Spheroids (MCTS). In order to complete *in vitro* photobiological studies, we next examined the photoactivity of SCV49 under deep-red light against 3D multicellular tumor spheroids (MCTS). This culture system is known to better mimic the *in vivo* tumor microenvironment compared to 2D monolayer cultures, closely reproducing key factors that influence PDT efficacy, such as nutrient and drug penetration, resistance to treatment, and hypoxic gradients toward the spheroid's core.⁶⁶ In this way, CT-26 MCTSs were incubated in the dark for 36 h with increasing concentrations of SCV49. After refreshing the medium, the spheroids were exposed to deep-red light (645 nm, 9 J cm⁻²) for 1 h. Following treatment, the shape, integrity, and diameter of the MCTSs were monitored over a 7-day period. Notably, as shown in Figure

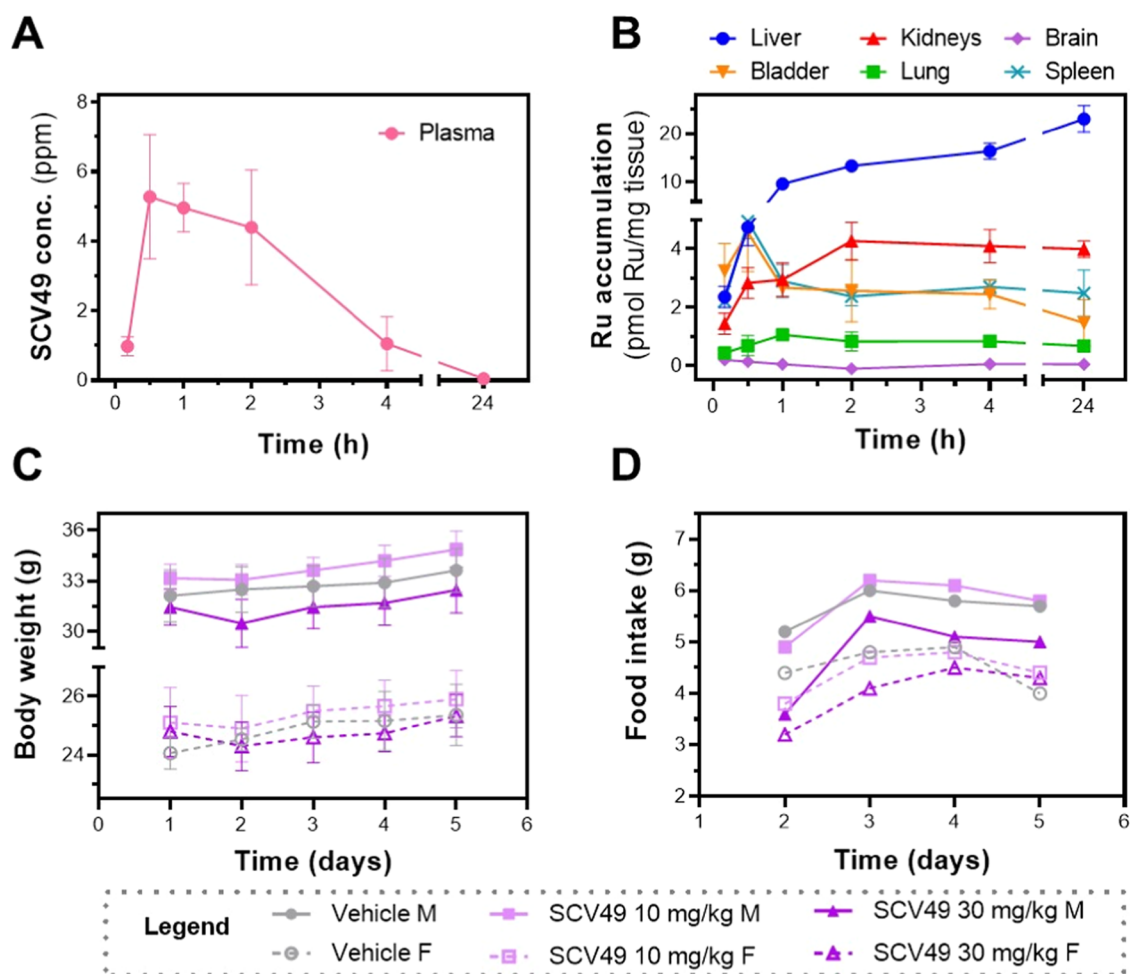


Figure 7. *In vivo* pharmacokinetic (PK) and toxicological evaluation of SCV49 in healthy CD1 mice. PK includes: (A) Plasma concentration–time curve, and (B) biodistribution profile of ruthenium (Ru) in major organs quantified by ICP-MS at various time points following IP administration of SCV49 at 5 mg/kg. Data are presented as mean \pm SD ($n = 3$ males). Toxicological evaluation includes: (C) Body weight (g) and (D) food intake (g/animal) of mice treated IP with vehicle or SCV49 (10 or 30 mg/kg) on day 1, with sacrifice on day 5. Data are presented as mean \pm SD ($n = 3$ males, $n = 3$ females).

6C,D, SCV49-treated MCTSs exhibited significant growth inhibition at concentrations above 10 μ M upon 645 nm irradiation compared to untreated MCTSs or those treated with lower concentrations of the compound.

Encouraged by the promising *in vitro* PDT activity of Ru-COUBPY complexes, specially under deep-red light irradiation, SCV49 was selected for *in vivo* safety and efficacy evaluation, which are key steps in the drug development process in the pharmaceutical industry. Our preclinical evaluation included pharmacokinetic studies, with a particular focus on plasma and tissue distribution as well as toxicity studies in healthy mice, alongside the assessment of *in vivo* PDT efficacy in tumor-bearing mice.

***In Vivo* Evaluation of the Pharmacokinetics and Toxicology of SCV49 in Healthy Mice.** The pharmacokinetic (PK) profile of SCV49 was evaluated in male CD1 mice following a single 5 mg/kg intraperitoneal (IP) dose, which is a common dose used in PK studies because it also provides information about drug tolerability. To that end, blood samples were collected for plasma analysis at specific time points (0.17, 0.5, 1, 2, 4, and 24 h) postadministration. Immediately afterward, the mice were sacrificed, perfused with PBS, and their organs harvested for further analysis. Plasma

samples were analyzed by UPLC-MS/MS at various time points to quantify SCV49 concentrations, enabling the construction of the plasma concentration–time curve and the calculation of PK parameters (Tables S10–S11 and Figure 7A). The analysis showed that SCV49 was rapidly absorbed, reaching a peak plasma concentration of 5.3 μ g/mL within 30 min, with levels stabilizing over the next 2 h (e.g., 4.4 μ g/mL at 2 h), indicating significant plasma exposure (AUC). The compound distributed well across tissues ($V_d = 1.04$ L/kg) and was steadily cleared from the body ($Cl = 0.20$ L/h·kg), with a moderate half-life of 3.63 h.

To gain insight into the biodistribution of SCV49 across various organs and its elimination pathway, the Ru content in key organs (i.e., liver, kidneys, spleen, bladder, lungs, and brain) was quantified using ICP-MS. Figure 7B shows the amount of Ru in each organ at various time points, while Figure S63 provides the percentage of Ru accumulated in each organ relative to the initial dose of SCV49 administered. Maximum accumulation in the spleen (0.44%), bladder (0.23%), lungs (0.20%), and brain (0.06%) was observed between 10 and 30 min postadministration. However, these values were considerably lower than those observed in the kidneys and liver. Maximum accumulation in the kidneys

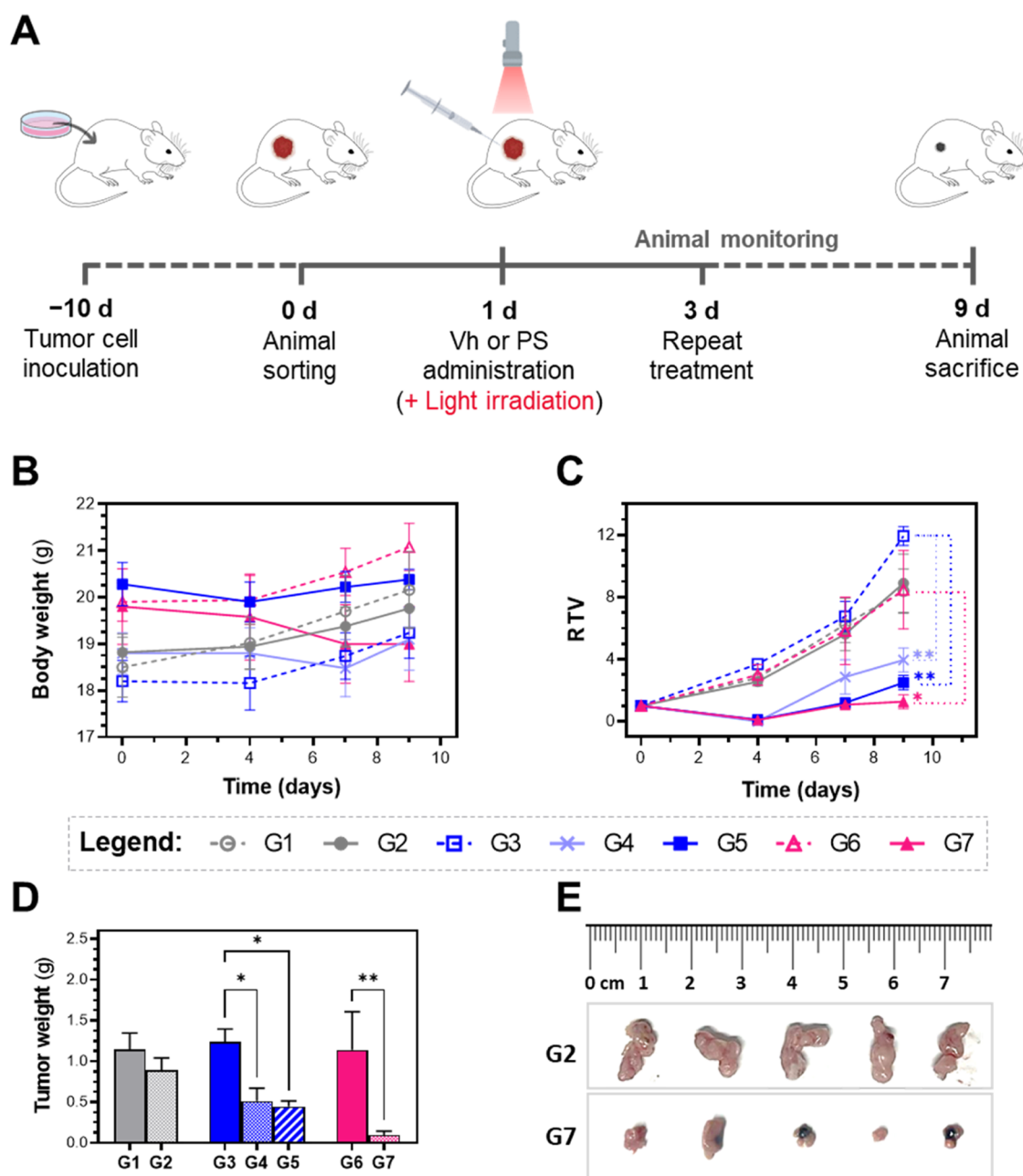


Figure 8. *In vivo* evaluation of SCV49 PDT antitumor efficacy in a subcutaneous CT-26 tumor model in BALB/c mice. (A) Experimental design: Eight-week-old female BALB/c mice were injected subcutaneously with 1.15×10^6 CT-26 cells on day -10 . By day 0, when tumors reached 50–100 mm³, mice were randomly divided into 7 groups ($n = 5$ /group, Table 4). On days 1 and 3, each group received the assigned treatment and was either exposed to light irradiation or not (660 nm, 15 or 20 min, Table 4, 100 mW/cm²). On day 9, animals were sacrificed, and organs and blood samples were collected. (B) Body weight (g) and (C) relative tumor volume (RTV) curves of mice over the 9-day study period. (D) Average tumor weights of mice on the day of sacrifice. Data are presented as mean \pm SEM ($n = 5$ females). RTV values on day 9, and average tumor weight data were analyzed using a one-way ANOVA followed by Bonferroni's multiple comparison test (Asterisks: * $p < 0.05$, ** $p < 0.001$). (E) Representative images of tumors from mice in group G2 (vehicle control, light 2x) and group G7 (SCV49, 6 mg/kg, light 2x) at the study endpoint.

(1.5%) was observed 4 h postadministration, followed by a decline that paralleled the plasma concentration–time profile, suggesting partial excretion of SCV49 or its metabolites via renal pathways. The accumulation in the liver steadily increased, reaching a peak (30.9%) at 24 h postadministration, by which time the compound had almost completely cleared from plasma. Accumulation in this organ is not surprising since compounds administered intraperitoneally first pass through the liver before entering the systemic circulation. Although

ICP-MS is the most used technique to assess metallodrug biodistribution, it measures only the total metal content and cannot differentiate between the parent compound and its metal-containing metabolites. Since SCV49 primarily accumulates in the liver, we suspected that its main clearance pathway might involve biliary excretion of the intact drug or its metabolites. To determine whether the detected Ru in the liver was from SCV49 or a metal-containing metabolite, we quantified the intact SCV49 in the liver at 1 and 24 h

Table 5. Experimental Groups of the *In Vivo* PDT Efficacy Study

group	item	conditions	dose/day (mg/kg)	administration schedule	irradiation schedule	light dose/administration (J cm ⁻²)
G1	vehicle	dark	-	2 times: day 1 and day 3	-	-
G2	vehicle	light	-	2 times: day 1 and day 3	2 times: 15 min each after 15 min of administration	90
G3	SCV49	dark	3	2 times: day 1 and day 3	-	-
G4	SCV49	light	3	2 times: day 1 and day 3	2 times: 15 min each after 15 min of administration	90
G5	SCV49	light	3	2 times: day 1 and day 3	4 times: 20 min each after 5 min of administration and on days 2 and 4	120
G6	SCV49	dark	6	2 times: day 1 and day 3	-	-
G7	SCV49	light	6	2 times: day 1 and day 3	2 times: 20 min each after 5 min of administration	120

postadministration using UPLC-MS/MS, which required developing a suitable bioanalytical method for liver matrices. As shown in Table S12, the UPLC-MS/MS results mirrored the trend observed in the ICP-MS study, confirming that intact SCV49 gradually accumulates in the liver. Notably, after 24 h, its levels were more than double those recorded at 1 h, suggesting that SCV49 is either metabolized very slowly in the liver or primarily excreted unmetabolized via the biliary pathway.

After completing the *in vivo* PK study at an IP dose of 5 mg/kg without any observed toxicity, we designed a 5-day toxicological study in male and female CD1 mice using three increasing doses: low (10 mg/kg), medium (30 mg/kg), and high (100 mg/kg). By systematically increasing the doses, we aimed to identify any dose-dependent toxic effects and establish a safe dosing range for future studies. Unfortunately, the higher dose could not be tested due to solubility problems during administration. Therefore, in this study, mice (3 per group) were intraperitoneally administered either vehicle (Vh) or SCV49 at 10 or 30 mg/kg (Table S13), and their food consumption and clinical signs were closely monitored. On day 5, blood samples were collected for hematological and plasma biochemical analysis. During necropsy, major organs (thymus, heart, spleen, liver, kidneys, reproductive organs, brain, lung, and bladder) were examined for toxicity markers, harvested, and weighed. Gratifyingly, both doses of SCV49 were well tolerated by mice of both sexes, with no mortality, clinical signs, or adverse effects observed during the 5-day study. Body weight and food consumption remained within the normal range of variability for the CD1 mice strain (Figures 7C,D and S64). Only one male and one female in the 30 mg/kg group experienced a temporary 4–5% body weight reduction on day 2, which recovered by day 5. Necropsy revealed no organ abnormalities at the 10 mg/kg dose, while all mice in the 30 mg/kg group exhibited slight lilac liver coloration, likely due to drug accumulation in the peritoneum. Again, UPLC-MS/MS analysis indicated that about 15% of the administered SCV49 dose remained in the liver by day 5. Surprisingly, ICP-MS analysis showed a lower total Ru accumulation of 6%. Regardless, these values, significantly lower than those observed at 24 h postadministration in the PK study, suggest that SCV49 is gradually cleared from the liver over time. Organ weight and organ weight/body weight ratios in both vehicle and SCV49 groups were generally within normal ranges (Figure S65). Blood samples were analyzed for changes in red blood cells, hemoglobin, hematocrit, platelets, white

blood cells, and related hematological parameters. No significant alterations were observed at either dose of SCV49 compared to the vehicle group (Figures S66–S67). Furthermore, biochemical analysis of plasma samples focused on hepatic and renal function parameters (Figure S68) revealed no significant differences between SCV49-treated and vehicle groups in markers such as albumin (ALB), aspartate aminotransferase, (AST) amylase (AMY), total bilirubin (TBIL) and blood urea nitrogen (BUN), indicating that the temporary accumulation of the PS in the liver and kidneys was not harmful to these organs. Additional metabolic markers, including glucose and cholesterol levels, further confirmed that the overall health of SCV49-treated animals was comparable to that of the controls. Thereby, the toxicological study showed that 10 and 30 mg/kg doses of SCV49 were well tolerated in both male and female CD1 mice over 5 days, with 30 mg/kg identified as the Maximum Tolerated Dose (MTD) in the absence of higher-dose testing.

***In Vivo* Evaluation of PDT Antitumoral Efficacy of SCV49 in a Mouse Subcutaneous CT-26 Syngeneic Colon Tumor Model.** After confirming the *in vivo* safety of SCV49 in healthy mice, we evaluated its PDT antitumor efficacy using a subcutaneous CT-26 syngeneic colon tumor model. Syngeneic models, which are generated after implanting tumor cells into genetically identical or near-identical mice, are particularly useful in cancer research because they maintain a fully functional immune system. Female BALB/c mice were inoculated with 1.15×10^6 CT-26 cells. Once tumors reached 50–100 mm³, the mice were divided into 7 groups (5 animals per group), each receiving a specific treatment as outlined in Figure 8A and Table 5. On days 1 and 3, 40 μ L of the vehicle or SCV49 (3 or 6 mg/kg) were administered intratumorally (IT) over 2 min to ensure even distribution (Figure S69). IT administration offers several advantages over systemic routes in preclinical evaluation but also in the clinic because it allows improved drug concentration in the target tumor tissue and reduces potential side effects due to accumulation in healthy tissues.⁶⁷ Based on the *in vitro* phototoxicity screening results, deep-red light (660 ± 20 nm, 100 mW/cm²; Figure S70) was used for irradiation in light-treated groups, with tumors irradiated for 15 (G2, G4) or 20 (G5, G7) min immediately following vehicle or drug administration, which corresponds to light doses of 90 and 120 J cm⁻², respectively (Table 5). Prior testing demonstrated that this irradiation schedule was well tolerated, causing no skin toxicity or clinical signs for one week post-treatment. Group G5 received additional irradiation on

days 2 and 4. Nonirradiated groups (G1, G3, G6) served as controls to assess tumor growth without light exposure, either after vehicle or SCV49 IT administration at 3 or 6 mg/kg doses.

Following the designated treatment and irradiation regimen, all animals were monitored for clinical signs and body weight changes, and tumor volumes were measured using a caliper. No mortality occurred during the 9-day observation period, and all animals showed normal behavior with no signs of stress or discomfort, consistent with previous PK and toxicological studies of CD1 healthy mice. As shown in Figure 8B, no significant differences in body weight or weight change were observed between SCV49-treated groups, whether exposed to light or not, and the vehicle groups. To illustrate the impact of different treatment regimens on tumor volume (mm^3), the relative tumor volume (RTV) is represented in Figure 8C. Mice treated with SCV49 (3 or 6 mg/kg) and irradiated with deep-red light showed significantly lower tumor volumes compared to nonirradiated groups, which displayed values similar to those of the vehicle-treated controls. Remarkably, on day 4, tumors in all irradiated SCV49-treated groups became unmeasurable (see Figure S71 for details of the images on day 4 for groups G1–G4) regardless of the compound dose and irradiation regime and light dose, indicating highly effective tumor destruction by the Ru-COUBPY complex upon irradiation. This result replicates the potent *in vitro* phototoxicity of SCV49 against CT-26 cells in an animal model. Comparison between groups G4 and G7 indicated that increasing the dose of the PS from 3 to 6 mg/kg and the light dose (from 90 to 120 J cm^{-2}) further enhanced tumor growth inhibition, with group G7 showing complete suppression of tumor regrowth after a slight recurrence on days 5–6. Group G5 (3 mg/kg, 4 consecutive irradiations with 120 J cm^{-2} dose) also achieved similar inhibition but caused skin ulcers in some animals due to the increased number of irradiations. On day 9, the tumor growth inhibition index (TGI, see SI for details), which compares PDT efficacy across treatment groups, confirmed superior efficacy in groups G5 (83%) and G7 (80%) compared with group G4 (69%). The *in vivo* PDT efficacy of SCV49 was further confirmed by the average tumor weight on day 9 (Figure 8D). Indeed, all SCV49-treated, light-irradiated groups showed a significant reduction in tumor weight compared to their nonirradiated counterparts, reaching statistical significance for all relevant comparisons between those groups in which only one variable was modified: G3 vs G4 (3 mg/kg, dark vs light, $2 \times 90 \text{ J cm}^{-2}$), G3 vs G5 (3 mg/kg, dark vs light, $4 \times 120 \text{ J cm}^{-2}$) and G6 vs G7 (6 mg/kg, dark vs light, $2 \times 120 \text{ J cm}^{-2}$). Consistent with tumor volume data, the 6 mg/kg group had significantly lower tumor weight than the 3 mg/kg light-treated groups, regardless of the irradiation schedule and light dose. Images of the tumors from groups 1 to 7 are depicted in Figures 8E and S72.

Finally, to assess the effects of the PDT treatment on animal health, plasma from SCV49-treated animals (6 mg/kg, dark and light groups) was subjected to biochemical analysis and compared with vehicle-treated groups. In addition to the parameters analyzed in the toxicological study (ALB, AMY, TBIL, BUN), four new parameters related to liver and kidney function were measured: alkaline phosphatase (ALP), alanine aminotransferase (ALT), creatinine (CRE) and total bile acid (TBA). As shown in Figure S73, no significant differences were found between SCV49-treated and vehicle groups, confirming

that PDT at 6 mg/kg did not affect hepatic or renal function. Other biochemical markers, including glucose, Na^+/K^+ ratio, Ca^{2+} , cholesterol, phosphorus, total protein, and globulin, were also within normal limits in both the SCV49- and vehicle-treated groups.

CONCLUSIONS

In this work, we described a new family of Ru(II) polypyridyl complexes incorporating unprecedented coumarin-based COUBPY ligands in the metal coordination sphere exhibiting potent *in vitro* cytotoxicity against cancer cells when irradiated with light within the phototherapeutic window under both normoxic (21% O_2) and hypoxic (2% O_2) conditions, while remaining nontoxic in the dark, leading to impressive phototoxic indices ($>30,000$). Besides singlet oxygen, Ru-COUBPY complexes are able to photogenerate Type I ROS (superoxide and hydroxyl radical), as confirmed by spectroscopic and EPR studies, thereby providing a distinct advantage over current marketed PSs based on the tetrapyrrolic scaffold that primarily rely on Type II PDT mechanism. Thus, the strong phototoxic activity of Ru-COUBPY complexes under hypoxic conditions arises from the coordination of the COUBPY ligands and their ability to photogenerate both Type I and Type II ROS in a key subcellular organelle (mitochondria). Importantly, the results from the *in vivo* safety and efficacy studies in mice underscore the potential of Ru-COUBPY PSs in the PDT treatment of cancer, particularly lead compound SCV49. On the one hand, SCV49 showed a favorable *in vivo* pharmacokinetics profile and excellent toxicological tolerability in healthy mice after IP administration as indicated by several parameters such as animal body weight, food consumption, organ weight, and exhaustive hematological and biochemical analysis. On the other hand, the outstanding *in vitro* phototoxicity of SCV49 against cancer cells was replicated in an animal model since a potent tumor inhibition in mice bearing subcutaneous CT-26 tumors was observed upon IT administration at doses as low as 3 mg/kg upon deep-red light irradiation (660 nm). Finally, it is worth noting that Ru-COUBPY PSs are highly photostable and aqueous-soluble and can be prepared in high purity from straightforward syntheses, which are highly desirable attributes for further clinical development. Overall, Ru-COUBPY complexes offer new opportunities for the PDT treatment of challenging hypoxic tumors by irradiation with light within the phototherapeutic window.

ASSOCIATED CONTENT

Supporting Information

The Supporting Information is available free of charge at <https://pubs.acs.org/doi/10.1021/jacs.4c15036>.

Experimental section; synthesis and chemical, photo-physical, and photochemical characterization of the compounds; computational studies; cellular uptake and *in vitro* (photo)cytotoxicity studies in 2D monolayer cells and in 3D MCTS; *in vivo* PK, toxicological and PDT efficacy studies in mice; and NMR and HRMS spectra (PDF)

AUTHOR INFORMATION

Corresponding Authors

Gilles Gasser – Chimie ParisTech, PSL University, CNRS, Institute of Chemistry for Life and Health Sciences,

Laboratory for Inorganic Chemical Biology, F-75005 Paris, France; orcid.org/0000-0002-4244-5097; Email: gilles.gasser@chimieparistech.psl.eu

Vicente Marchán – Departament de Química Inorgànica i Orgànica, Secció de Química Orgànica, Universitat de Barcelona (UB), and Institut de Biomedicina de la Universitat de Barcelona (IBUB), E-08028 Barcelona, Spain; orcid.org/0000-0002-1905-2156; Email: vmarchan@ub.edu

Authors

Diego Abad-Montero – Departament de Química Inorgànica i Orgànica, Secció de Química Orgànica, Universitat de Barcelona (UB), and Institut de Biomedicina de la Universitat de Barcelona (IBUB), E-08028 Barcelona, Spain

Albert Gandioso – Chimie ParisTech, PSL University, CNRS, Institute of Chemistry for Life and Health Sciences, Laboratory for Inorganic Chemical Biology, F-75005 Paris, France; orcid.org/0000-0002-5114-8502

Eduardo Izquierdo-García – Departament de Química Inorgànica i Orgànica, Secció de Química Orgànica, Universitat de Barcelona (UB), and Institut de Biomedicina de la Universitat de Barcelona (IBUB), E-08028 Barcelona, Spain; Chimie ParisTech, PSL University, CNRS, Institute of Chemistry for Life and Health Sciences, Laboratory for Inorganic Chemical Biology, F-75005 Paris, France; orcid.org/0000-0002-7253-6934

Sergi Chumillas – Departament de Química Inorgànica i Orgànica, Secció de Química Orgànica, Universitat de Barcelona (UB), and Institut de Biomedicina de la Universitat de Barcelona (IBUB), E-08028 Barcelona, Spain

Anna Rovira – Departament de Química Inorgànica i Orgànica, Secció de Química Orgànica, Universitat de Barcelona (UB), and Institut de Biomedicina de la Universitat de Barcelona (IBUB), E-08028 Barcelona, Spain

Manel Bosch – Unitat de Microscòpia Òptica Avançada, Centres Científics i Tecnològics, Universitat de Barcelona, E-08028 Barcelona, Spain; orcid.org/0000-0001-5870-6346

Mireia Jordà-Redondo – Institut Químic de Sarrià, Universitat Ramon Llull, E-08017 Barcelona, Spain

Davor Castaño – Departament de Química Inorgànica i Orgànica, Secció de Química Orgànica, Universitat de Barcelona (UB), and Institut de Biomedicina de la Universitat de Barcelona (IBUB), E-08028 Barcelona, Spain

Joaquín Bonelli – Departament de Química Inorgànica i Orgànica, Secció de Química Orgànica, Universitat de Barcelona (UB), and Institut de Biomedicina de la Universitat de Barcelona (IBUB), E-08028 Barcelona, Spain

Valentin V. Novikov – Departament de Química Inorgànica i Orgànica, Secció de Química Inorgànica, Universitat de Barcelona (UB), and Institute of Nanoscience and Nanotechnology of the University of Barcelona (IN2UB), E-08028 Barcelona, Spain; orcid.org/0000-0002-0225-0594

Alba Deyà – Health and Biomedicine Department, Leitat Technological Center, E-08225 Terrassa, Spain

José Luis Hernández – Health and Biomedicine Department, Leitat Technological Center, E-08225 Terrassa, Spain

Jorge Galino – Health and Biomedicine Department, Leitat Technological Center, E-08225 Terrassa, Spain

Marta E. Alberto – Dipartimento di Chimica e Tecnologie Chimiche, Università della Calabria, Arcavacata di Rende I-87036, Italy; orcid.org/0000-0001-9925-7233

Antonio Francés-Monerris – Institut de Ciència Molecular, Universitat de València, València 46071, Spain

Santi Nonell – Institut Químic de Sarrià, Universitat Ramon Llull, E-08017 Barcelona, Spain; orcid.org/0000-0002-8900-5291

Complete contact information is available at: <https://pubs.acs.org/10.1021/jacs.4c15036>

Author Contributions

◆D.A.-M., A.G., E.I.-G., and S.C. contributed equally to this work.

Notes

The authors declare the following competing financial interest(s): D.A.-M., A.G., E.I.-G., S.C., D.C., G.G. and V.M. are inventors of patent application PCT/EP2024/05431 (International publication number: WO2024/175605A1) protecting the COUBPY ligands and Ru-COUBPY complexes described in this work. The remaining authors have no conflicts of interest to declare.

ACKNOWLEDGMENTS

This work was supported by funds from the Spanish Ministerio de Ciencia, Innovación e Universidades-Agencia Estatal de Investigación (MICIU/AEI/10.13039/501100011033) (PID2020-117508RB-I00 and PID2023-146161OB-I00 to V.M.; PID2021-127554NA-I00 to A.F.-M.; PID2020-115801RB-C22 and PID2023-149483NB-C22 to S.N.), and by “ERDF A way of making Europe.” (PID2023-146161OB-I00 to V.M.; PID2021-127554NA-I00 to A.F.-M.; PID2023-149483NB-C22 to S.N.), the Generalitat de Catalunya-AGAUR (Llabor project 2021 LLAUV 00083 to V.M.), the Fundació Bosch i Gimpera (F2I-PdC_2022-007 to V.M.) and the Fundació “la Caixa” (CaixaImpulse Innovation project LCF/TR/CI23/56000013 to V.M.). D.A.-M. and A.R. were recipient fellows of the University of Barcelona (APIF). M.E.A. acknowledges the CINECA award under the ISCR initiative, for the availability of high-performance computing resources and support (IsCb6_IMPACTS project). A.F.-M. is grateful for the support of the Generalitat Valenciana (GV) through the project CIAICO/2022/121. S.N. thanks the Departament de Recerca i Universitats de la Generalitat de Catalunya for the support given to his research group (2021 SGR 01023) and the ICREA-Catalan Institution for Research and Advanced Studies for grant No. Ac2232308. This work was financially supported by an ERC Consolidator Grant Photo-MedMet to G. G. (GA 681679). A.G. thanks the ARC Foundation for cancer research for a postdoctoral research fellowship. E.I.-G. acknowledges support from a Margarita Salas postdoctoral grant at the University of Barcelona, funded by the Spanish Ministerio de Universidades with European Union funds—NextGenerationEU, and of the Fundació “la Caixa” for a postdoctoral contract associated with the project LCF/TR/CI23/56000013. The authors would like to thank Jordi Vilar and Dr. Judith Plaza for fruitful discussions and participation during the *in vivo* PK and toxicological studies performed at Draconis Pharma. The valuable collaboration of the technicians from the NMR, HRMS, ICP-MS, confocal microscopy, and EPR facilities of the Scientific and

Technological Centers (CCiTUB) of the Universitat de Barcelona is also appreciated.

REFERENCES

- (1) Chen, Z.; Han, F.; Du, Y.; Shi, H.; Zhou, W. Hypoxic microenvironment in cancer: molecular mechanisms and therapeutic interventions. *Signal Transduction Targeted Ther.* **2023**, *8*, No. 70.
- (2) Muz, B.; de la Puente, P.; Azab, F.; Azab, A. K. The role of hypoxia in cancer progression, angiogenesis, metastasis, and resistance to therapy. *Hypoxia* **2015**, *3*, 83–92.
- (3) Chowdhury, M.; Das, P. K. Hypoxia: Intriguing Feature in Cancer Cell Biology. *ChemMedChem* **2024**, *19*, No. e202300551.
- (4) Yuan, X.; Ruan, W.; Bobrow, B.; Carmeliet, P.; Eltzschig, H. K. Targeting hypoxia-inducible factors: therapeutic opportunities and challenges. *Nat. Rev. Drug Discovery* **2024**, *23*, 175–200.
- (5) Wang, X.; Peng, J.; Meng, C.; Feng, F. Fude, Recent advances for enhanced photodynamic therapy: from new mechanisms to innovative strategies. *Chem. Sci.* **2024**, *15*, 12234–12257.
- (6) Jiang, W.; Liang, M.; Lei, Q.; Li, G.; Wu, S. The Current Status of Photodynamic Therapy in Cancer Treatment. *Cancers* **2023**, *15*, No. 585.
- (7) Li, X.; Lovell, J. F.; Yoon, J.; Chen, X. Clinical development and potential of photothermal and photodynamic therapies for cancer. *Nat. Rev. Clin. Oncol.* **2020**, *17*, 657–674.
- (8) Dolmans, D. E. J. G. J.; Fukumura, D.; Jain, R. K. Photodynamic therapy for cancer. *Nat. Rev. Cancer* **2003**, *3*, 380–387.
- (9) Kessel, D.; Oleinick, N. L. Cell Death Pathways Associated with Photodynamic Therapy: An Update. *Photochem. Photobiol.* **2018**, *94*, 213–218.
- (10) Lu, B.; Wang, L.; Tang, H.; Cao, D. Recent advances in type I organic photosensitizers for efficient photodynamic therapy for overcoming tumor hypoxia. *J. Mater. Chem. B* **2023**, *11*, 4600–4618.
- (11) Zhang, C.; Hu, X.; Jin, L.; Lin, L.; Lin, H.; Yang, Z.; Huang, W. Strategic Design of Conquering Hypoxia in Tumor for Advanced Photodynamic Therapy. *Adv. Healthcare Mater.* **2023**, *12*, No. 2300530.
- (12) Li, G.; Wang, Q.; Liu, J.; Wu, M.; Ji, H.; Qin, Y.; Zhou, X.; Wu, L. Innovative strategies for enhanced tumor photodynamic therapy. *J. Mater. Chem. B* **2021**, *9*, 7347–7370.
- (13) Pham, T. C.; Nguyen, V.-N.; Choi, Y.; Lee, S.; Yoon, J. Recent Strategies to Develop Innovative Photosensitizers for Enhanced Photodynamic Therapy. *Chem. Rev.* **2021**, *121*, 13454–13619.
- (14) Zhao, X.; Liu, J.; Fan, J.; Chao, H.; Peng, X. Recent progress in photosensitizers for overcoming the challenges of photodynamic therapy: from molecular design to application. *Chem. Soc. Rev.* **2021**, *50*, 4185–4219.
- (15) Lan, M.; Zhao, S.; Liu, W.; Lee, C.-S.; Zhang, W.; Wang, P. Photosensitizers for Photodynamic Therapy. *Adv. Healthcare Mater.* **2019**, *8*, No. e1900132.
- (16) Li, X.; Kwon, N.; Guo, T.; Liu, Z.; Yoon, J. Innovative Strategies for Hypoxic-Tumor Photodynamic Therapy. *Angew. Chem., Int. Ed.* **2018**, *57*, 11522–11531.
- (17) Singh, P. P.; Sinha, S.; Gahtori, P.; Mishra, D. N.; Pandey, G.; Srivastava, V. Recent advancement in photosensitizers for photodynamic therapy. *Dyes Pigm.* **2024**, *229*, No. 112262.
- (18) Ju, M.; Yang, L.; Wang, G.; Zong, F.; Shen, Y.; Wu, S.; Tang, X.; Yu, D. A type I and type II chemical biology toolbox to overcome the hypoxic tumour microenvironment for photodynamic therapy. *Biomater. Sci.* **2024**, *12*, 2831–2840.
- (19) Chen, M.; Zhu, Q.; Zhang, Z.; Chen, Q.; Yang, H. Recent Advances in Photosensitizer Materials for Light-Mediated Tumor Therapy. *Chem. - Asian J.* **2024**, *19*, No. e202400268.
- (20) An, J.; Tang, S.; Hong, G.; Chen, W.; Chen, M.; Song, J.; Li, Z.; Peng, X.; Song, F.; Zheng, W.-H. An unexpected strategy to alleviate hypoxia limitation of photodynamic therapy by biotinylation of photosensitizers. *Nat. Commun.* **2022**, *13*, No. 2225.
- (21) Wang, R.; Li, X.; Yoon, J. Organelle-Targeted Photosensitizers for Precision Photodynamic Therapy. *ACS Appl. Mater. Interfaces* **2021**, *13*, 19543–19571.
- (22) Desai, V. M.; Choudhary, M.; Chowdhury, R.; Singhvi, G. Photodynamic therapy induced mitochondrial targeting strategies for cancer treatment: emerging trends and insights. *Mol. Pharmaceutics* **2024**, *21*, 1591–1608.
- (23) Yaqoob, M. D.; Xu, L.; Li, C.; Leong, M. M. L.; Xu, D. D. Targeting mitochondria for cancer photodynamic therapy. *Photodiagn. Photodyn. Ther.* **2022**, *38*, No. 102830.
- (24) Monro, S.; Colón, K. L.; Yin, H.; Roque, J.; Konda, P.; Gujar, S.; Thummel, R. P.; Lilge, L.; Cameron, C. G.; McFarland, S. A. Transition Metal Complexes and Photodynamic Therapy from a Tumor-Centered Approach: Challenges, Opportunities, and Highlights from the Development of TLD1433. *Chem. Rev.* **2019**, *119*, 797–828.
- (25) McFarland, S. A.; Mandel, A.; Dumoulin-White, R.; Gasser, G. Metal-based photosensitizers for photodynamic therapy: the future of multimodal oncology? *Curr. Opin. Chem. Biol.* **2020**, *56*, 23–27.
- (26) Gourdon, L.; Cariou, K.; Gasser, G. Phototherapeutic anticancer strategies with first-row transition metal complexes: a critical review. *Chem. Soc. Rev.* **2022**, *51*, 1167–1195.
- (27) Wu, Y.; Li, S.; Chen, Y.; He, W.; Guo, Z. Recent advances in noble metal complex based photodynamic therapy. *Chem. Sci.* **2022**, *13*, 5085–5106.
- (28) Karges, J. Clinical Development of Metal Complexes as Photosensitizers for Photodynamic Therapy of Cancer. *Angew. Chem., Int. Ed.* **2022**, *61*, No. e202112236.
- (29) Gandosio, A.; Purkait, K.; Gasser, G. Recent approaches towards the development of Ru(II) polypyridyl complexes for anticancer photodynamic therapy. *Chimia* **2021**, *75*, 845–855.
- (30) Munegowda, M. A.; Manalac, A.; Weersink, M.; McFarland, S. A.; Lilge, L. Ru(II) containing photosensitizers for photodynamic therapy: A critique on reporting and an attempt to compare efficacy. *Coord. Chem. Rev.* **2022**, *470*, No. 214712.
- (31) Conti, L.; Macedi, E.; Giorgi, C.; Valtancoli, B.; Fusi, V. Combination of light and Ru(II) polypyridyl complexes: Recent advances in the development of new anticancer drugs. *Coord. Chem. Rev.* **2022**, *469*, No. 214656.
- (32) Cole, H. D.; Vali, A.; Roque, J. A., III; Shi, G.; Kaur, G.; Hodges, R. O.; Francés-Monerris, A.; Alberto, M. E.; Cameron, C. G.; McFarland, S. A. Ru(II) Phenanthroline-Based Oligothienyl Complexes as Phototherapy Agents. *Inorg. Chem.* **2023**, *62*, 21181–21200.
- (33) Zheng, M.; Lin, X.; Xiong, K.; Zhang, X.; Chen, Y.; Ji, L.; Chao, H. A hetero-bimetallic Ru(II)-Ir(III) photosensitizer for effective cancer photodynamic therapy under hypoxia. *Chem. Commun.* **2024**, *60*, 2776–2779.
- (34) Feng, T.; Tang, Z.; Karges, J.; Shu, J.; Xiong, K.; Jin, C.; Chen, Y.; Gasser, G.; Ji, L.; Chao, H. An iridium(III)-based photosensitizer disrupting the mitochondrial respiratory chain induces ferritinophagy-mediated immunogenic cell death. *Chem. Sci.* **2024**, *15*, 6752–6762.
- (35) Liang, G.; Montesdeoca, N.; Tang, D.; Wang, B.; Xiao, H.; Karges, J.; Shang, K. Facile one-pot synthesis of Ir(III) Bodipy polymeric gemini nanoparticles for tumor selective NIR photoactivated anticancer therapy. *Biomaterials* **2024**, *309*, No. 122618.
- (36) Cole, H. D.; Roque, J. A.; Shi, G.; Lifshits, L. M.; Ramasamy, E.; Barrett, P. C.; Hodges, R. O.; Cameron, C. G.; McFarland, S. A. Anticancer Agent with Inexplicable Potency in Extreme Hypoxia: Characterizing a Light-Triggered Ruthenium Ubertoxin. *J. Am. Chem. Soc.* **2022**, *144*, 9543–9547.
- (37) Roque, J. A., III; Barrett, P. C.; Cole, H. D.; Lifshits, L. M.; Bradner, E.; Shi, G.; von Dohlen, D.; Kim, S.; Russo, N.; Deep, G.; Cameron, C. G.; Alberto, M. E.; McFarland, S. A. Os(II) Oligothienyl Complexes as a Hypoxia-Active Photosensitizer Class for Photodynamic Therapy. *Inorg. Chem.* **2020**, *59*, 16341–16360.
- (38) Steinke, S. J.; Dunbar, M. N.; Suarez, M. A. A.; Turro, C. Ru(II) Complexes with Absorption in the Photodynamic Therapy Window: $^1\text{O}_2$ Sensitization, DNA Binding, and Plasmid DNA Photocleavage. *Inorg. Chem.* **2024**, *63*, 11450–11458.
- (39) Kasparkova, J.; Hernández-García, A.; Kosthrunova, H.; Goicuría, M.; Novohradsky, V.; Bautista, D.; Markova, L.; Santana, M. D.; Brabec, V.; Ruiz, J. Novel 2-(5-Arylthiophen-2-yl)-benzoazole

Cyclometalated Iridium(III) dppz Complexes Exhibit Selective Phototoxicity in Cancer Cells by Lysosomal Damage and Oncosis. *J. Med. Chem.* **2024**, *67*, 691–708.

(40) Zamora, A.; Viguera, G.; Rodríguez, V.; Santana, M. D.; Ruiz, J. Cyclometalated iridium(III) luminescent complexes in therapy and phototherapy. *Coord. Chem. Rev.* **2018**, *360*, 34–76.

(41) Havrylyuk, D.; Hachey, A. C.; Fenton, A.; Heidary, D. K.; Glazer, E. C. Ru(II) photocages enable precise control over enzyme activity with red light. *Nat. Commun.* **2022**, *13*, No. 3636.

(42) Bonnet, S. Ruthenium-Based Photoactivated Chemotherapy. *J. Am. Chem. Soc.* **2023**, *145*, 23397–23415.

(43) Zhang, L.; Wang, P.; Zhou, X.-Q.; Bretin, L.; Zeng, X.; Husiev, Y.; Polanco, E. A.; Zhao, G.; Wijaya, L. S.; Biver, T.; Le Dévédec, S. E.; Sun, W.; Bonnet, S. Cyclic Ruthenium-Peptide Conjugates as Integrin-Targeting Phototherapeutic Prodrugs for the Treatment of Brain Tumors. *J. Am. Chem. Soc.* **2023**, *145*, 14963–14980.

(44) He, G.; He, M.; Wang, R.; Li, X.; Hu, H.; Wang, D.; Wang, Z.; Lu, Y.; Xu, N.; Du, J.; Fan, J.; Peng, X.; Sun, W. A Near-Infrared Light-Activated Photocage Based on a Ruthenium Complex for Cancer Phototherapy. *Angew. Chem., Int. Ed.* **2023**, *62*, No. e202218768.

(45) Zhang, C.; Qinc, W.-J.; Bai, X.-F.; Zhanga, X.-Z. Nanomaterials to relieve tumor hypoxia for enhanced photodynamic therapy. *Nano Today* **2020**, *35*, No. 100960.

(46) Huang, L.; Zhao, S.; Wu, J.; Yu, L.; Singh, N.; Yang, K.; Lan, M.; Wang, P.; Kim, J. S. Photodynamic therapy for hypoxic tumors: Advances and perspectives. *Coord. Chem. Rev.* **2021**, *438*, No. 213888.

(47) Wan, Y.; Fu, L.-H.; Li, C.; Lin, J.; Huang, P. Conquering the Hypoxia Limitation for Photodynamic Therapy. *Adv. Mater.* **2021**, *33*, No. 2103978.

(48) Gandioso, A.; Bresolí-Obach, R.; Nin-Hill, A.; Bosch, M.; Palau, M.; Galindo, A.; Contreras, S.; Rovira, A.; Rovira, C.; Nonell, S.; Marchán, V. Redesigning the Coumarin Scaffold into Small Bright Fluorophores with Far-Red to Near-Infrared Emission and Large Stokes Shifts Useful for Cell Imaging. *J. Org. Chem.* **2018**, *83*, 1185–1195.

(49) Rovira, A.; Pujals, M.; Gandioso, A.; López-Corrales, M.; Bosch, M.; Marchán, V. Modulating photostability and mitochondria selectivity in far-red/NIR emitting coumarin fluorophores through replacement of pyridinium by pyrimidinium. *J. Org. Chem.* **2020**, *85*, 6086–6097.

(50) Izquierdo-García, E.; Rovira, A.; Forcadell, J.; Bosch, M.; Marchán, V. Exploring Structural–Photophysical Property Relationships in Mitochondria-Targeted Deep-Red/NIR-Emitting Coumarins. *Int. J. Mol. Sci.* **2023**, *24*, No. 17427.

(51) Rovira, A.; Gandioso, A.; Goñalons, M.; Galindo, A.; Massaguer, A.; Bosch, M.; Marchán, V. Solid-phase approaches for labeling targeting peptides with far-red emitting coumarin fluorophores. *J. Org. Chem.* **2019**, *84*, 1808–1817.

(52) Izquierdo, E.; López-Corrales, M.; Abad-Montero, D.; Rovira, A.; Fabriàs, G.; Bosch, M.; Abad, J.-L.; Marchán, V. Fluorescently-labelled ceramides and 1-deoxyceramides: Synthesis, characterization and cellular distribution studies. *J. Org. Chem.* **2022**, *87*, 16351–16367.

(53) Ortega-Forte, E.; Rovira, A.; Gandioso, A.; Bonelli, J.; Bosch, M.; Ruiz, J.; Marchán, V. COUPY Coumarins as Novel Mitochondria-Targeted Photodynamic Therapy Anticancer Agents. *J. Med. Chem.* **2021**, *64*, 17209–17220.

(54) Bonelli, J.; Ortega-Forte, E.; Rovira, A.; Bosch, M.; Torres, O.; Cuscó, C.; Rocas, J.; Ruiz, J.; Marchán, V. Improving Photodynamic Therapy Anticancer Activity of a Mitochondria-Targeted Coumarin Photosensitizer Using a Polyurethane–Polyurea Hybrid Nanocarrier. *Biomacromolecules* **2022**, *23*, 2900–2913.

(55) Novohradsky, V.; Rovira, A.; Hally, C.; Galindo, A.; Viguera, G.; Gandioso, A.; Svitelova, M.; Bresolí-Obach, R.; Kostrhunova, H.; Markova, L.; Kasparkova, J.; Nonell, S.; Ruiz, J.; Brabec, V.; Marchán, V. Towards novel photodynamic anticancer agents generating superoxide anion radicals: A cyclometalated Ir(III) complex

conjugated to a far-red emitting coumarin. *Angew. Chem., Int. Ed.* **2019**, *58*, 6311–6315.

(56) Novohradsky, V.; Markova, L.; Kostrhunova, H.; Kasparkova, J.; Ruiz, J.; Marchán, V.; Brabec, V. A cyclometalated Ir(III) complex conjugated to a coumarin derivative is a potent photodynamic agent against prostate differentiated and tumorigenic cancer stem cells. *Chem. - Eur. J.* **2021**, *27*, 8547–8556.

(57) Rovira, A.; Ortega-Forte, E.; Hally, C.; Jordà-Redondo, M.; Abad-Montero, D.; Viguera, G.; Martínez, J. I.; Bosch, M.; Nonell, S.; Ruiz, J.; Marchán, V. Exploring Structure–Activity Relationships in Photodynamic Therapy Anticancer Agents Based on Ir(III)-COUPY Conjugates. *J. Med. Chem.* **2023**, *66*, 7849–7867.

(58) Ortega-Forte, E.; Rovira, A.; López-Corrales, M.; Hernández-García, A.; Ballester, F. J.; Izquierdo-García, E.; Jordà-Redondo, M.; Bosch, M.; Nonell, S.; Santana, M. D.; Ruiz, J.; Marchán, V.; Gasser, G. A near-infrared light-activatable Ru(II)-coumarin photosensitizer active under hypoxic conditions. *Chem. Sci.* **2023**, *14*, 7170–7184.

(59) Skripnikov, L. Chemissian 4.67 2020 www.chemissian.com.

(60) Martin, R. L. Natural transition orbitals. *J. Chem. Phys.* **2003**, *118*, 4775–4777.

(61) Plasser, F. TheoDORE: A toolbox for a detailed and automated analysis of electronic excited state computations. *J. Chem. Phys.* **2020**, *152*, No. 084108.

(62) Entradas, T.; Waldron, S.; Volk, M. The detection sensitivity of commonly used singlet oxygen probes in aqueous environments. *J. Photochem. Photobiol., B* **2020**, *204*, No. 111787.

(63) Roque, J. A., III; Cole, H. D.; Barrett, P. C.; Lifshits, L. M.; Hodges, R. O.; Kim, S.; Deep, G.; Francés-Monerris, A.; Alberto, M. E.; Cameron, C. G.; McFarland, S. A. Intraligand Excited States Turn a Ruthenium Oligothiophene Complex into a Light-Triggered Ubertoxin with Anticancer Effects in Extreme Hypoxia. *J. Am. Chem. Soc.* **2022**, *144*, 8317–8336.

(64) Teng, K.-X.; Chen, W.-K.; Niu, L.-Y.; Fang, W.-H.; Cui, G.; Yang, Q.-Z. BODIPY-Based Photodynamic Agents for Exclusively Generating Superoxide Radical over Singlet Oxygen. *Angew. Chem., Int. Ed.* **2021**, *60*, 19912–19920.

(65) Li, M.; Xia, J.; Tian, R.; Wang, J.; Fan, J.; Du, J.; Long, S.; Song, X.; Foley, J. W.; Peng, X. Near-Infrared Light-Initiated Molecular Superoxide Radical Generator: Rejuvenating Photodynamic Therapy against Hypoxic Tumors. *J. Am. Chem. Soc.* **2018**, *140*, 14851–14859.

(66) Friedrich, J.; Seidel, C.; Ebner, R.; Kunz-Schughart, L. A. Spheroid-based drug screen: considerations and practical approach. *Nat. Protoc.* **2009**, *4*, 309–324.

(67) Ma, C.-H.; Yang, J.; Mueller, J. L.; Huang, H.-C. Intratumoral Photosensitizer Delivery and Photodynamic Therapy. *Nano LIFE* **2021**, *11*, No. 2130003.

NOTE ADDED AFTER ASAP PUBLICATION

In Table 2, reactions 2 and 4, the first compound was corrected to read ${}^3\text{SCV}^{2+}$ on February 17, 2025.